Rho/Rok-dependent regulation of actomyosin contractility at tricellular junctions controls epithelial permeability in Drosophila

Thea Jacobs, Jone Isasti Sanchez, Steven Reger and Stefan Luschnig*

Institute of Integrative Cell Biology and Physiology, Cells in Motion (CiM) Interfaculty Center, University of Münster, Röntgenstrasse 16, D-48149 Münster

*Lead contact

Correspondence: luschnig@uni-muenster.de

Summary

Cell contacts in epithelia are remodeled to regulate paracellular permeability and to control passage of migrating cells, but how barrier function is modulated while preserving epithelial integrity is not clear. In the follicular epithelium of *Drosophila* ovaries, tricellular junctions (TCJs) open transiently in a process termed patency to allow passage of externally produced yolk proteins for uptake by the oocyte. Here we show that modulation of actomyosin contractility at cell vertices controls TCJ permeability. Before patency, circumferential actomyosin bundles are anchored at apical follicle cell vertices, where tension-sensing junctional proteins, Rho-associated kinase (Rok), and active Myosin II accumulate and maintain vertices closed. TCJ opening is initiated by redistribution of Myosin II from circumferential bundles to a medial pool, accompanied by decreasing tension on vertices. This transition requires activation of Cofilin-dependent F-actin disassembly by the phosphatase Slingshot and Myosin II inactivation by Myosin light chain phosphatase, and is counteracted by Rok. Accordingly, constitutive activation of Myosin or of Rho signaling prevent vertex opening, whereas reduced Myosin II or Rok activity cause excessive and premature vertex opening. Thus, opening of intercellular gaps in the follicular epithelium does not require actomyosin-based forces, but relies on a reduction of actomyosin contractility. Conversely, F-actin assembly is required for closing intercellular gaps after patency. Our findings are consistent with a force transduction model in which TCJ integrity is maintained by vertex-anchored contractile actomyosin. We propose that the cell-type-specific organization of actomyosin at cell vertices determines the mode of contractility-dependent regulation of epithelial permeability.

Introduction

Intercellular contacts in epithelia are dynamically remodeled to enable cell rearrangements, paracellular transport, or passage of migrating cells [1,2]. For instance, cell-cell contacts in the intestinal epithelium open transiently to enhance nutrient absorption after food intake [3]. Paracellular extravasation of leukocytes from blood vessels requires the transient opening of endothelial cell junctions stimulated by pro-inflammatory cytokines that modulate vascular endothelial (VE)-Cadherin-based adhesion [4]. Aberrant weakening or disassembly of intercellular junctions is a hallmark of infections and inflammatory conditions [5,6]. Transient paracellular leaks also occur during cell division and cell rearrangements in epithelia and are normally rapidly repaired by localized activation of Rho GTPases to promote actin polymerization and actomyosin-mediated contraction of junctions [7]. However, how epithelial cells modulate barrier function while preserving tissue integrity and undergoing dynamic shape changes during morphogenesis remains unclear.

Epithelial cells are connected by force-bearing adherens junctions (AJs) and by occluding junctions (tight junctions (TJs) in vertebrates and septate junctions (SJs) in invertebrates) that seal the intercellular space [1]. The most abundant intercellular contacts in epithelia are bicellular junctions (BCJs) between two cells. However, at sites where three or more cells meet (cell vertices), specialized tricellular junctions (TCJs) composed of a distinct set of proteins mediate adhesion and paracellular sealing [8]. In *Drosophila*, three TCJ-specific TM proteins, Anakonda (Aka; [9]), Gliotactin (Gli; [10]) and M6 [11] form the paracellular barrier along basolateral cell vertices, whereas the immunoglobulin domain TM protein Sidekick (Sdk) localizes at apical tricellular AJs (tAJs) and is required for efficient cell rearrangements [12–15]. Vertebrate epithelia display tricellular tight junctions (tTJs; [16]) that differ structurally from invertebrate TCJs and comprise TM proteins of the Angulin/Lipolysis-stimulated Lipoprotein Receptor (LSR) family [17] and the MARVEL family TM protein Tricellulin [18].

Cell vertices are key points that sense and integrate forces in epithelial and endothelial tissues [19]. They are dynamically remodeled during cell rearrangements [20] and play fundamental roles in cytoskeletal organization, mitotic spindle orientation, and epithelial barrier function [21]. Moreover, TCJs provide preferred routes for leukocyte extravasation from blood vessels [22] and are exploited by bacterial pathogens for breaching epithelial barriers [23]. However, despite their crucial functions, how TCJs are assembled and remodeled is only beginning to be understood.

Studies in *Drosophila* have revealed important insights into the molecular mechanisms underlying epithelial cell polarization and intercellular junction formation [1,24]. *Drosophila* ovaries contain chains of developing follicles, each of which comprises 16 germline cells encased by an epithelial monolayer of somatic follicle cells (FCs; Fig. 1A). TCJs in the follicular epithelium overlying the oocyte open transiently during vitellogenesis to generate intercellular channels

88 that allow passage of externally produced yolk proteins for uptake by the oocyte [25,26]. The
89 opening of FC vertices, referred to as follicular patency [27,28], is initiated by the sequential
90 removal of adhesion proteins (E-Cad, N-Cad, NCAM/Fasciclin 2, Sdk) from FC vertices and
91 by actomyosin remodeling [29,30]. However, the mechanisms underlying TCJ opening and the
92 role of actomyosin-based forces in this process were not clear.

93 We show here that vertex-anchored actomyosin generates tensile forces that keep TCJs
94 closed before patency. This depends on Rho-associated kinase (Rok), a main effector of Rho
95 GTPase [31,32]. Rok regulates actomyosin contractility in mammalian cells by phosphorylating
96 non-muscle Myosin II (MyoII) regulatory light chain (MRLC), thus activating MyoII, and by
97 inhibitory phosphorylation of Myosin light-chain phosphatase (MLCP), which normally
98 inactivates MyoII [31,33]. In parallel, Rok regulates F-actin dynamics by phosphorylating and
99 thereby activating LIM-domain kinase 1 (LIMK1), which in turn inactivates the F-actin-severing
100 protein Cofilin [34–36]. We found that in *Drosophila* FCs, Rok is required to maintain active MyoII,
101 but not for regulating F-actin dynamics via the LIMK1-Cofilin pathway. At the onset of patency,
102 downregulation of Rok results in MyoII inactivation and decreased tension acting on vertices.
103 In parallel, the protein phosphatase Slingshot (Ssh; [37]) activates Cofilin-dependent F-actin
104 disassembly. This work reveals how actomyosin contractility at TCJs is modulated to control
105 epithelial permeability.

106

107 **Results**

108 **Actomyosin organization at follicle cell vertices**

109 TCJs in the main body follicle epithelium overlying the oocyte open during vitellogenesis
110 (stages 8-10; Fig. 1A; [25]) to generate patent intercellular channels, which are visualized by
111 incubating follicles in fluorescent dextran (Fig. 1B; [29]). Intercellular gaps first appear at stage
112 9, reach maximal width at stage 10A, and close at stage 11 (Fig. 1B; [29,30]). To understand the
113 mechanism of vertex opening, we investigated the distribution of actomyosin in main body FCs
114 at the onset of patency (Fig. 1C-E).

115 **Reorganization of apical actomyosin precedes vertex opening**

116 We visualized E-Cadherin (E-Cad::RFP), non-muscle Myosin II (MyoII::GFP) and the
117 mechanosensitive protein Vinculin (Vinc::GFP) in living follicles before (stages 7 and 8) and
118 during early (stage 9) and full patency (stage 10A; Fig. 1C-E). On the basal side of FCs, MyoII
119 was enriched in planar polarized stress fibers throughout the stages analyzed (Fig. 1C; [38,39]).
120 By contrast, on the apical side of FCs in pre-patent follicles (stages 7 and 8), MyoII (Fig. 1D)
121 and actin filaments (visualized by Lifeact::mBaoJin; Fig. S1A,B) aligned at the cell perimeter,

with prominent accumulations at TCJs. MyoII bundles appeared to connect to vertices, where Vinc was enriched overlapping with E-Cad (Fig. 1D,E), suggesting that actomyosin bundles exert tension on AJs at cell vertices. While E-Cad was present in continuous belt-like AJs on the apical side at stage 7, E-Cad was removed from vertices at stage 8 (Fig. 1D). At onset of patency (stage 9), MyoII receded from vertices and redistributed from circumferential bundles to a medial pool (Fig. 1D; [40]). Apical MyoII levels further decreased by stage 10A, while basal MyoII-containing stress fibers were maintained (Fig. 1D). Concurrently, Vinc accumulations at apical vertices decreased by 74.7% (n(st8)=9, n(st9)=10, p=0.00026) from stage 8 to stage 9 and disappeared at stage 10A (Fig. 1E). Similarly, the force-sensing LIM-domain proteins Ajuba (GFP::Jub) and Zyxin (Zyx::GFP) [41] accumulated in distinct puncta adjacent to apical vertices at stage 8 and disappeared by stage 9 (Fig. S1C-F). These findings suggest that apical FC vertices are under tension in pre-patent follicles and that tension on vertices decreases at the onset of patency.

To explain these results, we considered a force transduction model [19,42–44] in which contractile actomyosin bundles make end-on connections to AJs at vertices (Fig. 1G). The combined forces acting on these AJs are directed towards the center and tighten the vertex. Conversely, reduced actomyosin-based tension at stage 9 is predicted to release tension and thereby allow opening of vertices for patency.

Tension on vertices decreases at the onset of patency

To test this model, we asked whether vertices in pre-patent FCs are indeed under tension. We laser-ablated apical FC vertices (marked by E-Cad::GFP) at stage 7, 8 or 9, and analyzed displacement of neighboring vertices as a measure for tension acting on them (Fig. S2A,B; Video S1). This revealed rapid displacement in stage 7 (0.0114 +/- 0.0063 µm/s) and stage 8 (0.0097 +/- 0.0048 µm/s) follicles. By contrast, displacement was strongly reduced (0.0038 +/- 0.0023 µm/s) at stage 9 (Fig. S2B-D), consistent with results from ablations of bicellular junctions [40]. These findings, along with the behavior of force-sensing proteins (Fig. S1), indicate that FC vertices are under tension in pre-patent follicles and suggest that tension on vertices decreases before the onset of patency.

Rho-associated kinase localizes at follicle cell vertices and limits vertex opening

To understand how tension on vertices is generated, we analyzed the distribution of Rok, a key regulator of actomyosin contractility [32,33]. We found that an mNeonGreen::Rok fusion protein (mNG::Rok; [45]) accumulates at apical cell boundaries, with prominent puncta abutting FC vertices in pre-patent follicles (Fig. 2A). Like Rok, active MyoII, detected by an antibody against MRLC phosphorylated on Serine 21 (p-MyoII), accumulated near apical vertices in pre-patent follicles (Fig. 2B). Rok puncta disappeared by the onset of patency at stage 9 (Fig.

157 2A,E), resembling the behavior of tension-sensing proteins Vinc, Jub, and Zyx (Fig. 1E, Fig.
158 S1). Along with mNG::Rok, p-MyoII accumulations receded from vertices towards the medial
159 region at stage 9, suggesting that Rok maintains a pool of active MyoII at vertices. Supporting
160 this idea, RNAi-mediated depletion of Rok in FC clones led to a substantial reduction (57.9%
161 of control (st. 8); n=11, p=0.000881) of p-MyoII signals at vertices (Fig. 2C,F). Rok-depleted
162 cells showed enlarged apical outlines, indicating reduced apical constriction, as reported
163 previously [40,46]. Strikingly, Rok-depleted FC clones also displayed enlarged dextran-filled
164 intercellular gaps (quantified as the fraction of total cell area, referred to as patency index [29];
165 Fig. 2D,G). Intercellular gaps in Rok-depleted tissue occasionally appeared already at stage
166 8, preceding the onset of patency in neighboring control tissue (Fig. 2D). Thus, Rok-dependent
167 MyoII activity is required to limit both the extent and the timing of vertex opening.

168 **Downregulation of Myosin II activity by protein phosphatase 1 is required for patency**

169 We asked next how Rok regulates MyoII activity in FCs. Rok can activate Myosin by
170 phosphorylating MRLC and by inhibiting Myosin light chain phosphatase (MLCP, also known
171 as protein phosphatase 1 (PP1); Fig. 3E), which inactivates MyoII by dephosphorylating MRLC
172 [33]. We found that loss of the PP1 catalytic subunit, PP1β, encoded by *flapwing (flw*; [47,48]), in
173 *flw*^{FP41} FC clones caused excessive MyoII activation (indicated by elevated p-MyoII levels) in
174 pre-patent follicles (Fig. 3A,B). MyoII hyperactivation in *flw*^{FP41} clones persisted into stage 10A,
175 when apical p-MyoII levels are low in wild-type FCs (Fig. 3A,B), suggesting that PP1β normally
176 inactivates apical MyoII at the onset of patency. *flw*^{FP41} cells showed smaller apical areas
177 compared to control cells, presumably due to increased apical constriction upon MyoII
178 overactivation. Strikingly, FC vertices in *flw*^{FP41} clones failed to open when surrounding wild-
179 type epithelium was fully patent at stage 10A (Fig. 3C,D), indicating that MyoII inactivation by
180 PP1β is required for FCs to enter patency. Conversely, interfering with MyoII activity by
181 expressing in FCs a dominant-negative form of Myosin II heavy chain lacking the actin-binding
182 head domain (MHC^{DN}::YFP; [49]) caused reduced MyoII phosphorylation (Fig. 3G) and
183 excessive vertex opening (Fig. 3F,H). Together, these findings indicate that Rok-dependent
184 MyoII contractility acts to keep FC vertices closed until stage 9, while subsequent
185 downregulation of MyoII activity by MLCP is necessary to allow vertex opening, the extent of
186 which is determined by the degree of MyoII activity.

187 **Rok controls patency by regulating Myosin II activity**

188 Besides promoting MyoII contractility, Rok stimulates F-actin assembly in mammalian cells by
189 activating LIMK1, which in turn inhibits the F-actin-severing activity of Cofilin [34–36]. To test
190 whether Rok-dependent F-actin regulation is involved in vertex remodeling, we analyzed the
191 effects of *Rok* RNAi on F-actin in FCs. Surprisingly, while *Rok* RNAi led to substantially
192 reduced apical p-MyoII signals (Fig. 2C), there was only a minor reduction of F-actin in Rok-

193 depleted cells at stage 7 and no significant effect on the distribution or levels of F-actin at later
194 stages (Fig. 2C,F). Notably, F-actin still accumulated at apical junctions in Rok-depleted cells
195 (Fig. 2C). These findings suggest that in FCs Rok acts mainly by controlling MyoII activity,
196 whereas Rok-dependent regulation of F-actin dynamics via LIMK1 appears to play no
197 significant role. Consistent with this notion, loss of LIMK1 in homozygous viable *LIMK1*^{2} null
198 mutants [50] had no detectable effect on F-actin organization in FCs or on patency (Fig. S3).

199 **Vertex-associated F-actin prevents TCJ opening**

200 F-actin was enriched at apical FC vertices in pre-patent follicles (stages 7, 8) and receded from
201 vertices by stage 9 (Fig. S1A,B), suggesting that initiation of patency involves F-actin
202 remodeling. To test this idea, we used mutations or RNAi to probe the roles of F-actin-
203 regulators. However, in many cases this led to pleiotropic effects on epithelial organization or
204 cell survival (not shown), thus precluding specific functions in patency. Therefore, to deplete
205 F-actin in a more acute fashion, we treated cultured follicles with Latrunculin A (LatA), which
206 prevents actin assembly by sequestering actin monomers and by accelerating F-actin
207 depolymerization [51]. In follicles treated with LatA for 45 minutes, apical F-actin was strongly
208 reduced compared to controls (Fig. 4A,B) and E-Cad-labelled AJs were interrupted at vertices
209 (Fig. 4D). Interestingly, LatA treatment led to enlarged intercellular gaps on the apical, but not
210 basolateral side, at stage 10A (Fig. 4C-E), suggesting that an apical pool of LatA-sensitive F-
211 actin is required to maintain E-Cad at vertices and to prevent precocious vertex opening.

212 **Enabled/VASP is dispensable for vertex-associated F-actin assembly in FCs**

213 A key F-actin regulator, Enabled / vasodilator-stimulated protein (Ena/VASP), promotes
214 assembly of vertex-associated F-actin in mammalian cells [52] and in *Drosophila* [53,54]. A
215 GFP::Ena fusion protein localized, besides cytoplasmic accumulations, to puncta abutting FC
216 vertices in pre-patent follicles (Fig. S4A,B), resembling Jub, Vinc, and Zyx localization (Fig.1E,
217 Fig. S1C,D), and consistent with direct binding of Ena to Vinc and Zyx [55]. The GFP::Ena puncta
218 disappeared from vertices by stage 9 (Fig. S4A,B), coinciding with a reduction of vertex-
219 associated F-actin (Fig. S1A,B). To probe Ena´s role in organizing this F-actin pool, we
220 depleted Ena function either by sequestrating Ena protein at mitochondria (Fig. S4D; [53,56]) or
221 by inducing FC clones homozygous for a newly generated *ena* deletion allele (*ena*$^{1.8}$; Fig.
222 S4C,E). Both led to depletion of Ena protein but had no or only slight effects on F-actin
223 accumulation at apical vertices (Fig. S4D,E,G), and patency was not detectably affected (Fig.
224 S4H,I). By contrast, Ena overexpression caused excessive F-actin accumulation and formation
225 of actin-rich-protrusions at apical cell boundaries and vertices (Fig. S4F,G). Thus, although
226 Ena can induce vertex-associated F-actin assembly in FCs, it is dispensable for this function,
227 presumably due to redundancy with other factors.

228 **Hypertonic shock induces opening of vertices *ex vivo***

229 Searching for ways to analyze the dynamics of patency, we noticed that treatment of cultured
230 stage 9 follicles with hypertonic medium induced transient opening of FC vertices, resembling
231 the intercellular gaps observed during patency (Fig. 5A; [29]). Addition of PBS or sucrose to the
232 medium induced rapid formation of intercellular gaps, which reached maximal size after
233 approximately one minute and closed after 5 minutes (n=5; Fig. 5A,B; Video S2). Addition of
234 DMSO had a more gradual effect, and caused an initial contraction of cells, followed by
235 opening of vertices with a peak at seven minutes and closure after 25 minutes (n=8; Fig. 5A,B;
236 Video S2). By contrast, hypotonic treatment by diluting (1:1) the medium with water did not
237 alter cell contacts at stage 9 (Fig. 5A,B; n=8) but induced closure of intercellular gaps in patent
238 (stage 10A) follicles (Fig 5C,D; n=5). Interestingly, opening of vertices upon DMSO-induced
239 hypertonic treatment was restricted to vitellogenic (stage 9) follicles, and was not observed at
240 earlier stages (Fig. 5E,F). In previtellogenic follicles (stage 5) with proliferating FCs, transient
241 gaps were observed only at boundaries of dividing cells (Fig. 5E; Video S3), revealing
242 junctional remodeling during mitosis [57]. These findings suggest that hypertonic treatment can
243 induce opening of FC vertices only when remodeling of cell-cell junctions and of actomyosin
244 has provided a permissive condition for initiation of patency.

245 We used the hypertonic (DMSO-induced) shock assay in stage 9 follicles as a proxy for
246 patency initiation to probe the roles of F-actin in vertex opening and closure. Cortical F-actin
247 (visualized by Lifeact::GFP) increased 10 sec after adding DMSO, coinciding with initial
248 contraction of FCs (Fig. 5G; Video S4). Subsequently, F-actin disappeared from the cortex as
249 intercellular gaps became visible and re-appeared at vertices when gaps started to close.
250 Interestingly, Lifeact::GFP signals were anti-correlated with intercellular gap size: minimal
251 signals concurred with maximal gap size and vice versa (Fig. 5H), suggesting that disassembly
252 of cortical F-actin may be required for vertex opening, while F-actin assembly may promote
253 closure of gaps.

254 **Cofilin-dependent F-actin disassembly is required for opening intercellular gaps**

255 To test this hypothesis, we manipulated F-actin dynamics using pharmacological inhibitors or
256 genetics and analyzed gap opening and closure following DMSO-induced hypertonic shock.
257 In follicles treated with LatA, Lifeact::GFP signals were uniformly low and did not change after
258 adding DMSO, although FCs contracted after 3 minutes (Fig. 5G,I; Video S5). Intercellular
259 spaces in LatA-treated follicles opened, with gaps reaching maximal size after 16 minutes, but,
260 unlike controls, failed to close within one hour (Fig. 5G,I), consistent with a requirement of F-
261 actin assembly for vertex closure.

262 Conversely, FC clones lacking the protein phosphatase Slingshot (Ssh; [37]), which promotes F-
263 actin disassembly by dephosphorylating and thereby activating Cofilin, showed substantial

accumulation of apical F-actin that persisted into stage 10A (Fig. 4F,G). Interestingly, *ssh*$^{1-11}$ mutant FC clones displayed reduced intercellular openings during patency (Fig. 4H,I). Taken together, these results indicate that Slingshot/Cofilin-dependent F-actin disassembly is required for vertex opening, while F-actin assembly promotes closure of gaps after patency.

Acute activation of Rho signaling is sufficient to prevent patency

Our findings suggest that Rho-induced actomyosin contractility is necessary to maintain FC vertices closed. To test whether Rho signaling is also sufficient to prevent vertex opening, we combined the hypertonic shock assay (Fig. 5) with the CRY2/CIBN optogenetic system [58] to acutely activate Rho signaling (Fig. 6A). We generated mosaic follicles co-expressing CRY2-RhoGEF2::mCherry and plasma membrane-anchored CIBN::pmGFP in FC clones (Fig. 6B). Illumination with blue light (488 nm) triggered rapid plasma membrane recruitment of CRY2-RhoGEF2::mCherry. When a hypertonic shock was applied by adding DMSO nine minutes after optogenetic Rho activation, control cells opened their vertices, whereas vertices remained closed in FCs with activated Rho signaling (Fig. 6B,C). As a control, chronic membrane localization of Rho in flies expressing CRY2-RhoGEF2::mCherry and CIBN::pmGFP under constant light blocked patency, whereas CRY2-RhoGEF2::mCherry expressed alone was distributed in the cytoplasm and did not affect patency (Fig. 6D,E). Thus, the blockade of patency after optogenetic Rho activation is not caused by chronic RhoGEF2 overexpression, and acute activation of Rho-induced actomyosin contractility is sufficient to prevent opening of FC vertices.

Discussion

We used follicular patency in *Drosophila* as a model to understand how an intact epithelial barrier is transiently breached by opening of TCJs to enhance paracellular permeability. Our work reveals that this process is governed by modulation of actomyosin contractility at cell vertices. We show first that before patency, apical vertex-anchored actomyosin bundles generate tensile forces that keep vertices closed. Sustained MyoII activity in pre-patent follicles depends on Rho-associated kinase, which accumulates at vertices along with tension-sensing junctional proteins Jub, Vinc, and Zyx. Second, when TCJ opening initiates, MyoII redistributes from vertex-anchored peripheral bundles to a medial pool, Rok and tension-sensing proteins withdraw from vertices, and junctional tension is released. Third, this transition requires inactivation of MyoII by Myosin light-chain phosphatase (MLCP), which is normally inactivated through phosphorylation by Rok. Removal of Rok at the onset of patency abrogates inactivation of MLCP, enabling it to inactivate MyoII, thereby releasing constricting forces and allowing vertices to open. Finally, we show that a dynamic (LatA-sensitive) pool of F-actin is

299 associated with apical FC vertices and helps to keep vertices closed. Initiation of patency
300 requires Slingshot/Cofilin-dependent disassembly of this F-actin network. Conversely, F-actin
301 assembly is required for closing intercellular gaps after patency.

302 Thus, surprisingly, opening of intercellular gaps in the follicular epithelium does not require
303 actomyosin-based forces, but depends on reduction of actomyosin contractility, which acts to
304 constrict vertices. This is consistent with a force transduction model in which TCJ integrity is
305 maintained by contractile actomyosin bundles that are anchored in an end-on fashion at
306 vertices (Fig. 1G; [19,42–44]). This type of actomyosin arrangement was described in mammalian
307 mammary epithelial EpH4 cells, where the tricellular tight junction (tTJ) protein Tricellulin
308 regulates F-actin organization through Cdc42 [59] and anchors actin filaments at vertices via α-
309 Catenin, which in turn recruits Vinculin to reinforce linkage to the tTJ-associated actin network
310 [52]. Resembling our findings in *Drosophila*, MyoII is concentrated at tTJs and is required for
311 maintaining tTJ integrity in EpH4 cells [52]. While Tricellulin is not conserved in *Drosophila*, the
312 vertex-specific adhesion protein Sidekick (Sdk) plays an analogous role by recruiting MyoII [15],
313 suggesting that MyoII has a common function in TCJ maintenance in vertebrate and
314 invertebrate epithelia.

315 **Tension-sensitive actomyosin assembly at cell vertices**

316 What mediates the assembly of vertex-anchored F-actin? Tension-sensitive Vinculin
317 recruitment promotes F-actin organization at vertices and is required for TCJ integrity and
318 barrier function in mammalian cells [52] and in the *Xenopus* epidermis [60]. Although Vinculin also
319 accumulates at vertices of pre-patent follicles, we found Vinculin to be dispensable for F-actin
320 organization and for control of patency (not shown), consistent with earlier reports of *vinc* being
321 a non-essential gene in *Drosophila* [61,62]. This could be explained by functional redundancy of
322 Vinculin with other proteins that mediate tension-sensitive linkage between AJs and F-actin,
323 such as Ajuba and Zyxin [63]. Interestingly, Vinculin and Zyxin recruit the actin polymerase
324 Ena/VASP [55] to AJs under tension, where Ena promotes F-actin assembly [64]. Ena is recruited
325 to vertices in *Drosophila* (Fig. S4; [53,54,65]) and in mammalian epithelial cells [52]. However, like
326 Vinculin, Ena was not essential for F-actin assembly in FCs, suggesting that Ena acts in a
327 redundant fashion along with other factors that ensure robust maintenance of this F-actin
328 network.

329 **Dual regulation of actomyosin contractility during patency**

330 Work in mammalian cells suggested that tensile forces sustain a positive feedback loop that
331 generates vertex-anchored actin filaments through tension-dependent recruitment of Vinculin
332 and actin-polymerizing proteins, such as Ena/VASP [52,64]. We showed that local activation of
333 MyoII by vertex-localized Rok generates contractile forces, which in turn may promote tension-

334 dependent F-actin assembly at FC vertices. Our genetic results indicate that this feedback
335 loop can be broken by inactivating MyoII through MLCP or by promoting Ssh/Cofilin-dependent
336 F-actin disassembly (Fig. 6F). Thus, patency initiation involves dual regulation of actomyosin
337 contractility, and both, MyoII inactivation and F-actin disassembly, are required for normal
338 vertex opening. Interestingly, we identified two phosphatases, MLCP and Slingshot, as
339 essential regulators of these processes during patency initiation. It will be interesting to
340 elucidate whether Rho/Rok signaling regulates both phosphatases to jointly control F-actin
341 dynamics and Myosin activity, or whether different upstream signals are involved. While Rok
342 clearly controls MyoII activity via MLCP in pre-patent FCs, our genetic results suggest that the
343 conserved parallel pathway downstream of Rok that regulates F-actin dynamics via LIMK1-
344 dependent inactivation of Cofilin [34,36,66] is not active in FCs. Instead, we found that the
345 phosphatase Ssh is essential for Cofilin-dependent F-actin disassembly at the onset of
346 patency. As Ssh has not been reported to be regulated by Rho signaling, it will be interesting
347 to elucidate how Ssh activity or localization is controlled in FCs. Interestingly, the mammalian
348 Ssh homolog SSH1L can antagonize Rok signaling by dephosphorylating the Rok substrate
349 MyoII phosphatase MYPT-1 [67]. While it is not known whether Ssh acts analogously in
350 *Drosophila*, such a mechanism could mediate coordinate regulation of actin disassembly and
351 Myosin inactivation in patency initiation.

352 We showed that F-actin reassembly is required for sealing intercellular gaps to terminate
353 patency. Similarly, localized transient Rho activation mediates actin polymerization and Rok-
354 dependent contractility to repair tight junction leaks in *Xenopus* epidermis [7]. How Rho activity
355 is spatially and temporally regulated to restore barrier integrity, or to control TCJ opening, as
356 in the case of patency, is not clear. In vertebrate endothelial cells, inflammatory mediators,
357 such as histamine, thrombin, or VEGF, induce opening of cell-cell junctions to increase
358 vascular permeability by activating actomyosin contractility through RhoA [68]. Thus, in this
359 system, opposite to *Drosophila* follicles or *Xenopus* epidermis, Rho-induced actomyosin
360 contractility increases junctional permeability rather than preventing it. In endothelial cells,
361 which differ from cuboidal epithelia in cell shape and cytoskeletal organization, Rho activation
362 induces radially aligned stress fibers that exert pulling and shear forces on VE-Cadherin-based
363 junctions, resulting in junctional leaks [69,70]. By contrast, contractility of vertex-anchored
364 actomyosin filaments in FCs maintains TCJ integrity and prevents premature TCJ opening.
365 Thus, the cell-type-specific organization of actomyosin at cell vertices determines the mode of
366 contractility-dependent regulation of epithelial permeability.

367

368 **Materials and Methods**

369 ***Drosophila* strains and genetics**

370 Unless noted otherwise, *Drosophila* strains are described in FlyBase. Genotypes of specimens
371 shown in the figures are listed in Table S1. All strains used in this work are listed in Table S2.

372 Mosaic follicles carrying mutant clones for *ena*$^{1.8}$, *flw* ^{FP41}, or *ssh*$^{1-11}$ were generated using
373 Flipase-induced mitotic recombination. A strain carrying a *hs-Flp* source and the appropriate
374 FRT chromosome marked with either *ubi-GFP-nls* or *ubi-mRFP-nls* transgenes was crossed
375 to a strain carrying the mutation of interest on the corresponding FRT chromosome. To induce
376 Flp-mediated mitotic recombination, progeny of these crosses was heat-shocked at the pupal
377 stage (48-96 hours after puparium formation) for 3 x 60 mins at 37°C in a water bath. For RNAi-
378 mediated knockdown or overexpression experiments, flip-out clones were generated by
379 crossing flies carrying *hs-Flp*^{122} and the UAS construct of choice to flies carrying an
380 *act5C>CD2>Gal4* flip-out construct. Progeny of these crosses was heat-shocked as adults (1-
381 2 days after eclosion) for 30 min at 37°C in a water bath.

382 **Generation of new *ena* alleles**

383 A transgenic CRISPR approach was used to generate *ena* deletion alleles. Male flies
384 expressing from a transgene (B-83021) two different guide RNAs (sgRNA-WKO.1-C12.1,
385 sgRNA-WKO.1-C12.2; [71]) targeting the *ena* coding sequence were crossed to females
386 expressing *nos*-Cas9 in the germline. F1 males expressing *nos-Cas9* and the two guide RNAs
387 were crossed with *y w; Gla/CyO Dfd-GMR-YFP* females to establish stocks. Single F2 males
388 were mated with *ena*^{23}*/CyO* (B-25405) females to test for complementation of *ena*^{23} lethality.
389 Lines were established from crosses that failed to complement lethality. The *ena*$^{1.8}$ mutation
390 was recombined onto an FRTG13 chromosome for subsequent mosaic analyses. To identify
391 lesions in the *ena* locus of newly induced *ena* alleles, genomic DNA was isolated from
392 homozygous embryos (detected by the absence of YFP signal from the *CyO Dfd-GMR-YFP*
393 balancer chromosome) and the *ena* genomic region was amplified using oligonucleotides (5'-
394 CCTGGTACACATTCGCGTTT and 5'-TGTGCAGCTGAGATCTTGGA) and sequenced.

395 **Transgenic constructs**

396 The UAS-Lifeact::mBaoJin construct was generated as follows. The Lifeact peptide [72] coding
397 sequence was produced by annealing two complementary oligonucleotides (5'-
398 CAAAATGGGCGTGGCCGATCTGATCAAGAAGTTCGAGAGCATCAGCAAGGAGGAA and
399 5'-
400 CCGGTTCCTCCTTGCTGATGCTCTCGAACTTCTTGATCAGATCGGCCACGCCCATTTTG
401 GTAC), resulting in a dsDNA fragment with overhangs compatible with AgeI and XbaI
402 restriction sites, respectively. A plasmid carrying the mBaoJin [73] coding sequence was a gift
403 from Kiryl Piatkevich (Westlake University, Zhejiang, China). The mBaoJin coding sequence
404 was amplified using forward (5'-GAACCGGTCGCCACCGTGTCGAAAGGTGAAGAGGA) and

405 reverse (5'-GATCTAGATTATTTGTACAGCTCGTCCATGC) primers and the product was cut
406 with AgeI and XbaI. The Lifeact and mBaojin fragments were co-ligated with pUASt-attB [74]
407 after cutting with AgeI and XbaI. The pUASt-Lifeact::mBaoJin construct was integrated into the
408 attP40 and attP2 landing sites, respectively, using PhiC31-mediated site-specific integration
409 [74]. All plasmids used in this study are listed in Table S2.

410 **Antibodies and immunostainings**

411 Female flies were collected 24-48 hours after eclosion and were fed on baker´s yeast for two
412 days before dissecting ovaries in Shields and Sang M3 medium (Biomol; supplemented with
413 1x Penicillin/Streptomycin and 10% fetal bovine serum; M3++ medium). For immunostaining,
414 dissected ovarioles were fixed in 4% PFA in PBS for 15 minutes at room temperature, rinsed
415 quickly 3 times in PBT and blocked 3 x 30 minutes in 10% BSA in PBT (0.2% Tween-20).
416 Primary antibodies (see Table S3) were diluted in 10% BSA in PBT and incubated with slow
417 agitation overnight at 4°C. After 3 washes in PBT, samples were blocked 3 x 30 mins in 10%
418 BSA/PBT. Fluorophore-conjugated secondary antibodies (see Table S3) were added at 1:500
419 in 10% BSA/PBT and incubated for 2.5 hours at room temperature or overnight at 4°C. After
420 six washes (10 min each) in PBT, samples were mounted in ProLong Gold antifade medium
421 (Thermo Fisher).

422 For anti-phospho-Myosin stainings, follicles were dissected in M3++ medium and then fixed in
423 4% PFA in PBS supplemented with phosphatase inhibitor solution (modified after [75]).
424 Subsequent steps were done as described above, except that primary antibodies were
425 incubated for 24 hours at 4°C. Phosphatase inhibitor solution was prepared as a 20x stock
426 solution (modified after [75]: 20 mM NaF, 20 mM β-Glycerophosphate, 20 mM Na_3VO_4, 100 mM
427 $Na_4P_2O_7 \cdot 10H_2O$).

428 F-actin in fixed samples was visualized using Phalloidin AlexaFluor-488 or Phalloidin
429 AlexaFluor-568 (1:1000; Fisher Scientific), together with secondary antibodies.

430 **Culture and imaging of ovarian follicles**

431 For live imaging, follicles were dissected and cultured in M3++ medium. For plasma membrane
432 staining, CellMask Orange Plasma Membrane Stain (6.25 µg/mL final concentration; Thermo
433 Fisher) was added to the dissection medium. For permeability assays, follicles were
434 transferred to 200 µL M3++ medium containing dextran (10 kDa) conjugated with AlexaFluor-
435 647 (37.5 µg/mL, Life Technologies). For visualizing F-actin with Lifeact-Halo2, follicles
436 expressing *UAS-Lifeact-Halo2* [76] driven by *GR1*-Gal4 were incubated in M3++ medium
437 containing 1 µM HALO-Tag Ligand-Janelia Fluor-646 (Promega, GA1120) for 20 minutes
438 before mounting. Follicles were imaged immediately after mounting on glass slides with cover
439 slips.

440 For osmotic treatment, dissected follicles were transferred to 8-well glass-bottom chambers
441 (VWR 734-2061) coated with Poly-D-Lysine (1 mg/mL in 0.15 M H_3BO_3 pH 8.4). Each chamber
442 contained 200 µL M3++ medium supplemented with dextran-AlexaFluor647 as above.
443 Osmolarity was changed during imaging by adding the respective osmotic agent as follows:
444 10 µL 50% DMSO in M3++ (final concentration 2.38% DMSO or 304 mosmol/L); 10 µL 5x PBS
445 in M3++ (final concentration 0.238x PBS or 88,96 mosmol/L); 50 µL 250 mM Sucrose in M3++
446 (final concentration 50 mM or 50 mosmol/L). For hypotonic shocks, 150 µL H_2O were added
447 to follicles in 150 µL medium containing dextran-AlexaFluor647. The concentration of dextran-
448 AlexaFluor647 (37.5 µg/mL) was kept constant during osmotic shocks by adding the
449 appropriate amount of dextran-AlexaFluor647 along with the osmotic reagent.

450 For Latrunculin A treatment, follicles were dissected and incubated for 45 minutes in M3++
451 medium supplemented with Insulin (0.4 mg/mL; Sigma I0516) and Latrunculin A (2 µM; Abcam
452 #ab144290).

453 For long-term high-resolution live imaging, follicles were mounted in fibrinogen gel as
454 described in [77]. Follicles were dissected in serum-free M3 medium containing Fibrinogen (5
455 mg/mL; Sigma F3879) and transferred in 7 µL of medium to a MatTek round dish imaging
456 chamber (MatTek Corp., P35G-1.5-14-C). Fibrinogen was clotted by adding 1.6 µL Thrombin
457 (1000 units/mL; Sigma T4648) for 5 to 10 minutes. The clot was covered with 200 µL
458 Schneider's medium supplemented with 20% fetal bovine serum, Glucose (1 g/L) and Insulin
459 (0.4 mg/mL; Sigma I0516; adapted from [77]).

460 For osmotic shock experiments, follicles were transferred to 8-well glass-bottom chambers
461 (VWR 734-2061) coated with Poly-D-Lysine (1 mg/mL in 0.15 M H_3BO_3 pH 8.4). Each chamber
462 contained 200 µL M3++ medium supplemented with 10 kDa dextran-AlexaFluor647 as above.

463 For optogenetic experiments, flies were fed on yeast in constant darkness at 25°C for two days
464 before dissection. Flies were dissected and samples were mounted under red light before
465 imaging on a Leica SP8 confocal microscope.

466 For all remaining experiments, follicles were mounted in M3++ medium (containing dextran-
467 AlexaFluor647 where applicable) on glass slides with cover slips held by spacers (a cut cover
468 slip between two layers of double-sided tape).

469 All media and reagents are listed in Table S4.

470 **Laser Ablations**

471 Dissected follicles were mounted in eight-well glass-bottom chambers coated with poly-D-
472 Lysine and covered with 200 µL M3++ medium. Imaging was performed on a Zeiss Spinning
473 Disk (Yokogawa CSU-X1) confocal microscope with 100x / NA 1.45 oil immersion objective.

Images of a single z-plane were acquired at a rate of two frames per second over 40 seconds. Ablations were performed using a pulsed 355 nm laser (Rapp OptoElectronics). Vertices were ablated within a 5-pixel ROI with one laser pulse (530 ms) per vertex. Vertex displacement was tracked in FIJI using the Manual Tracking Plugin (https://imagej.net/ij/plugins/track/track.html). Using R (v4.2.3, with RStudio Interface (2023.03.0+386)), the displacement of the three vertices next to the ablated vertex was calculated as Euclidean distance ($d = \sqrt{(x_1 - y_1)^2 + (x_2 - y_2)^2}$). The mean displacement and standard deviation of the three vertices per movie were calculated and the time series data was smoothed by applying a running median with a median window of k=5.

Microscopy

Confocal images were acquired on a Leica SP8 confocal microscope with 40x / NA 1.3 or 63x / NA 1.4 oil immersion objectives or on a Zeiss LSM980 confocal microscope equipped with an Airyscan 2 module and a 63x / NA 1.4 oil immersion objective. Airyscan images were processed using Zeiss Zen blue (v3.5.093.00010) Software with super-resolution filter set to 6.3.

Image analysis

Images were processed using FIJI/ImageJ (v1.42; [78]) and OMERO (5.8.0). Image panels were assembled using OMERO.figure v6.2.2 [79] and Affinity Designer (v2.3.0).

For quantification of signal intensities at vertices, average projections of 20 confocal sections spanning 3 µm of the apical region were generated. Fluorescence intensities at vertices were measured within circular ROIs with 60 pixels diameter (for 63 x objective) or 55 pixels diameter (40 x objective) centered on a vertex. Background was subtracted and mean intensities were normalized to the mean intensities at the earliest stage analyzed.

To measure patency index, confocal sections of main body FCs were acquired at 25% of total epithelium height from the basal surface. A median filter was applied to the dextran-AlexaFluor647 channel, and a threshold was set to create a mask of the dextran signal. The Analyze Particle feature in FIJI was used to measure the area filled with dextran signal. The patency index represents the total area of dextran-filled intercellular spaces within the ROI divided by the total ROI area [29].

Statistics

Statistical analyses were performed in R (4.2.3) using RStudio Interface (2023.03.0+386). For phenotypic analyses, sample size (n) was not predetermined using statistical methods, but was chosen by considering the variability of a given phenotype, determined by the standard deviation. Sample size for each experiment is indicated in the graphs or figure legends.

Experiments were considered independent if specimens were derived from different parental crosses. Investigators were not blinded to allocation during experiments. The data was tested for normality using the Shapiro-Wilk test. Welch's two-sample t-test was used for normally distributed data. For data that was not normally distributed, or data that was compared between multiple stages, the Wilcoxon rank-sum test (R standard package) was used. P-values were corrected for multiple testing using the Bonferroni-Holm method [80].

Acknowledgements

We thank Wilko Backer for expert technical help, Konrad Basler, Yohanns Bellaïche, Nick Brown, Stefano De Renzis, Katja Röper, Antoine Guichet, Veit Riechmann and Frank Schnorrer for providing antibodies and fly stocks, and Kiryl Piatkevich for sharing the mBaoJin plasmid. We acknowledge service by the Münster Imaging Network, the Developmental Studies Hybridoma Bank (created by the NICHD of the NIH and maintained at the University of Iowa), and the Bloomington Drosophila Stock Center (NIH P40OD018537). This work was supported by the Deutsche Forschungsgemeinschaft (SFB 1348 "Dynamic Cellular Interfaces"), the "Cells-in-Motion" Cluster of Excellence (EXC 1003-CiM), and the University of Münster.

Author contributions

Conceptualization, T.J., J.I.S., S.L.; Methodology, all authors; Investigation, all authors; Formal Analysis, T.J., J.I.S., S.R.; Visualization, T.J., J.I.S., S.R.; Reagents and tools, all authors; Figures, T.J., S.L.; Writing – Original Draft, T.J.; Writing – Review and Editing, S.L.; Funding Acquisition, S.L; Supervision, S.L.

Declaration of interests

The authors declare no competing interests.

Supplemental information

Document S1. Figures S1–S4 and Tables S1-S3.

Video S1. Laser ablations of apical FC vertices. Related to Figure 1 and S2.

Video S2. Osmotic treatment of cultured follicles. Related to Figure 4 and 5.

Video S3. Hypertonic treatment of stage 5 follicles containing cells in interphase and mitotic cells. Related to Figure 4 and 5.

Video S4. Hypertonic treatment of follicle expressing Lifeact::GFP. Related to Figure 4 and 5.

Video S5. Hypertonic treatment of follicle expressing Lifeact::GFP treated with Latrunculin A. Related to Figure 4 and 5.

Video S6. Optogenetic activation of Rho signaling followed by hypertonic treatment. Related to Figure 6.

References

1. Mira-Osuna, M., and Borgne, R.L. (2024). Assembly, dynamics and remodeling of epithelial cell junctions throughout development. Development *151*, dev201086. https://doi.org/10.1242/dev.201086.

2. Varadarajan, S., Stephenson, R.E., and Miller, A.L. (2019). Multiscale dynamics of tight junction remodeling. J Cell Sci *132*. https://doi.org/10.1242/jcs.229286.

3. Madara, J.L., and Pappenheimer, J.R. (1987). Structural basis for physiological regulation of paracellular pathways in intestinal epithelia. J. Membrane Biol. *100*, 149–164. https://doi.org/10.1007/BF02209147.

4. Vestweber, D. (2015). How leukocytes cross the vascular endothelium. Nature Reviews Immunology *15*, 692–704. https://doi.org/10.1038/nri3908.

5. Guttman, J.A., and Finlay, B.B. (2009). Tight junctions as targets of infectious agents. Biochimica et Biophysica Acta (BBA) - Biomembranes *1788*, 832–841. https://doi.org/10.1016/j.bbamem.2008.10.028.

6. Shen, L., Weber, C.R., Raleigh, D.R., Yu, D., and Turner, J.R. (2011). Tight Junction Pore and Leak Pathways: A Dynamic Duo. Annu. Rev. Physiol. *73*, 283–309. https://doi.org/10.1146/annurev-physiol-012110-142150.

7. Stephenson, R.E., Higashi, T., Erofeev, I.S., Arnold, T.R., Leda, M., Goryachev, A.B., and Miller, A.L. (2019). Rho Flares Repair Local Tight Junction Leaks. Dev Cell *48*, 445-459 e5. https://doi.org/10.1016/j.devcel.2019.01.016.

8. Higashi, T., and Chiba, H. (2020). Molecular organization, regulation and function of tricellular junctions. Biochimica et Biophysica Acta (BBA) - Biomembranes *1862*, 183143. https://doi.org/10.1016/j.bbamem.2019.183143.

9. Byri, S., Misra, T., Syed, Z.A., Bätz, T., Shah, J., Boril, L., Glashauser, J., Aegerter-Wilmsen, T., Matzat, T., Moussian, B., et al. (2015). The Triple-Repeat Protein Anakonda Controls Epithelial Tricellular Junction Formation in Drosophila. Dev Cell *33*, 535–548. https://doi.org/10.1016/j.devcel.2015.03.023.

10. Schulte, J., Tepass, U., and Auld, V.J. (2003). Gliotactin, a novel marker of tricellular junctions, is necessary for septate junction development in Drosophila. J Cell Biol *161*, 991–1000. https://doi.org/10.1083/jcb.200303192.

11. Zappia, M.P., Brocco, M.A., Billi, S.C., Frasch, A.C., and Ceriani, M.F. (2011). M6 Membrane Protein Plays an Essential Role in Drosophila Oogenesis. PLoS ONE *6*, e19715. https://doi.org/10.1371/journal.pone.0019715.

12. Finegan, T.M., Hervieux, N., Nestor-Bergmann, A., Fletcher, A.G., Blanchard, G.B., and Sanson, B. (2019). The tricellular vertex-specific adhesion molecule Sidekick facilitates polarised cell intercalation during Drosophila axis extension. PLoS Biol *17*, e3000522. https://doi.org/10.1371/journal.pbio.3000522.

13. Letizia, A., He, D., Astigarraga, S., Colombelli, J., Hatini, V., Llimargas, M., and Treisman, J.E. (2019). Sidekick Is a Key Component of Tricellular Adherens Junctions that Acts to Resolve Cell Rearrangements. Dev Cell *50*, 313-326 e5. https://doi.org/10.1016/j.devcel.2019.07.007.

14. Lye, C.M., Naylor, H.W., and Sanson, B. (2014). Subcellular localisations of the CPTI collection of YFP-tagged proteins in Drosophila embryos. Development *141*, 4006–4017. https://doi.org/10.1242/dev.111310.

15. Uechi, H., and Kuranaga, E. (2019). The Tricellular Junction Protein Sidekick Regulates Vertex Dynamics to Promote Bicellular Junction Extension. Dev Cell *50*, 327-338 e5. https://doi.org/10.1016/j.devcel.2019.06.017.

16. Furuse, M., Izumi, Y., Oda, Y., Higashi, T., and Iwamoto, N. (2014). Molecular organization of tricellular tight junctions. Tissue Barriers *2*, e28960. https://doi.org/10.4161/tisb.28960.

17. Masuda, S., Oda, Y., Sasaki, H., Ikenouchi, J., Higashi, T., Akashi, M., Nishi, E., and Furuse, M. (2011). LSR defines cell corners for tricellular tight junction formation in epithelial cells. J Cell Sci *124*, 548–555. https://doi.org/10.1242/jcs.072058.

18. Ikenouchi, J., Furuse, M., Furuse, K., Sasaki, H., Tsukita, S., and Tsukita, S. (2005). Tricellulin constitutes a novel barrier at tricellular contacts of epithelial cells. Journal of Cell Biology *171*, 939–945. https://doi.org/10.1083/jcb.200510043.

19. Higashi, T., and Miller, A.L. (2017). Tricellular junctions: how to build junctions at the TRICkiest points of epithelial cells. Mol Biol Cell *28*, 2023–2034. https://doi.org/10.1091/mbc.E16-10-0697.

20. Sugimura, K., and Otani, T. (2024). Vertex remodeling during epithelial morphogenesis. Current Opinion in Cell Biology *91*, 102427. https://doi.org/10.1016/j.ceb.2024.102427.

21. Bosveld, F., Wang, Z., and Bellaiche, Y. (2018). Tricellular junctions: a hot corner of epithelial biology. Curr Opin Cell Biol *54*, 80–88. https://doi.org/10.1016/j.ceb.2018.05.002.

22. Burns, A.R., Walker, D.C., Brown, E.S., Thurmon, L.T., Bowden, R.A., Keese, C.R., Simon, S.I., Entman, M.L., and Smith, C.W. (1997). Neutrophil transendothelial migration is independent of tight junctions and occurs preferentially at tricellular corners. The Journal of Immunology *159*, 2893–2903.

23. Sumitomo, T., Nakata, M., Higashino, M., Yamaguchi, M., and Kawabata, S. (2016). Group A Streptococcus exploits human plasminogen for bacterial translocation across epithelial barrier via tricellular tight junctions. Sci Rep *6*, 1–13.

24. Buckley, C.E., and St Johnston, D. (2022). Apical–basal polarity and the control of epithelial form and function. Nat Rev Mol Cell Biol. https://doi.org/10.1038/s41580-022-00465-y.

25. Berg, C., Sieber, M., and Sun, J. (2023). Finishing the egg. GENETICS, iyad183. https://doi.org/10.1093/genetics/iyad183.

26. Raikhel, A.S., and Dhadialla, T.S. (1992). Accumulation of yolk proteins in insect oocytes. Annual Review of Entomology *37*, 217–251. https://doi.org/10.1146/annurev.en.37.010192.001245.

27. Patchin, S., and Davey, K.G. (1968). The histology of vitellogenesis in Rhodnius prolixus. J Insect Physiol *14*, 1815–1820.

28. Pratt, G.E., and Davey, K.G. (1972). The corpus allatum and oogenesis in Rhodnius prolixus. I The effects of allatectomy. Journal of Experimental Biology *56*, 201–214.

29. Isasti-Sanchez, J., Münz-Zeise, F., Lancino, M., and Luschnig, S. (2021). Transient opening of tricellular vertices controls paracellular transport through the follicle epithelium during Drosophila oogenesis. Dev Cell *56*, 1083-1099.e5. https://doi.org/10.1016/j.devcel.2021.03.021.

30. Row, S., Huang, Y.-C., and Deng, W.-M. (2021). Developmental regulation of oocyte lipid intake through “patent” follicular epithelium in Drosophila melanogaster. iScience *24*, 102275. https://doi.org/10.1016/j.isci.2021.102275.

31. Amano, M., Ito, M., Kimura, K., Fukata, Y., Chihara, K., Nakano, T., Matsuura, Y., and Kaibuchi, K. (1996). Phosphorylation and Activation of Myosin by Rho-associated Kinase (Rho-kinase)*. Journal of Biological Chemistry *271*, 20246–20249. https://doi.org/10.1074/jbc.271.34.20246.

32. Ishizaki, T., Maekawa, M., Fujisawa, K., Okawa, K., Iwamatsu, A., Fujita, A., Watanabe, N., Saito, Y., Kakizuka, A., Morii, N., et al. (1996). The small GTP-binding protein Rho binds to and activates a 160 kDa Ser/Thr protein kinase homologous to myotonic dystrophy kinase. EMBO J *15*, 1885–1893.

33. Kimura, K., Ito, M., Amano, M., Chihara, K., Fukata, Y., Nakafuku, M., Yamamori, B., Feng, J., Nakano, T., Okawa, K., et al. (1996). Regulation of Myosin Phosphatase by Rho and Rho-Associated Kinase (Rho-Kinase). Science *273*, 245–248. https://doi.org/10.1126/science.273.5272.245.

34. Maekawa, M., Ishizaki, T., Boku, S., Watanabe, N., Fujita, A., Iwamatsu, A., Obinata, T., Ohashi, K., Mizuno, K., and Narumiya, S. (1999). Signaling from Rho to the actin cytoskeleton through protein kinases ROCK and LIM-kinase. Science *285*, 895–898. https://doi.org/10.1126/science.285.5429.895.

35. Ohashi, K., Hosoya, T., Takahashi, K., Hing, H., and Mizuno, K. (2000). A Drosophila Homolog of LIM-Kinase Phosphorylates Cofilin and Induces Actin Cytoskeletal Reorganization. Biochemical and Biophysical Research Communications *276*, 1178–1185. https://doi.org/10.1006/bbrc.2000.3599.

36. Yang, N., Higuchi, O., Ohashi, K., Nagata, K., Wada, A., Kangawa, K., Nishida, E., and Mizuno, K. (1998). Cofilin phosphorylation by LIM-kinase 1 and its role in Rac-mediated actin reorganization. Nature *393*, 809–812. https://doi.org/10.1038/31735.

37. Niwa, R., Nagata-Ohashi, K., Takeichi, M., Mizuno, K., and Uemura, T. (2002). Control of Actin Reorganization by Slingshot, a Family of Phosphatases that Dephosphorylate ADF/Cofilin. Cell *108*, 233–246. https://doi.org/10.1016/S0092-8674(01)00638-9.

38. He, L., Wang, X., Tang, H.L., and Montell, D.J. (2010). Tissue elongation requires oscillating contractions of a basal actomyosin network. Nat Cell Biol *12*, 1133–1142. https://doi.org/10.1038/ncb2124.

39. Valencia-Expósito, A., Grosheva, I., Míguez, D.G., González-Reyes, A., and Martín-Bermudo, M.D. (2016). Myosin light-chain phosphatase regulates basal actomyosin oscillations during morphogenesis. Nat Commun *7*, 10746. https://doi.org/10.1038/ncomms10746.

40. Balaji, R., Weichselberger, V., and Classen, A.K. (2019). Response of Drosophila epithelial cell and tissue shape to external forces in vivo. Development *146*, dev171256. https://doi.org/10.1242/dev.171256.

41. Anderson, C.A., Kovar, D.R., Gardel, M.L., and Winkelman, J.D. (2021). LIM domain proteins in cell mechanobiology. Cytoskeleton *78*, 303–311. https://doi.org/10.1002/cm.21677.

42. Choi, W., Acharya, B.R., Peyret, G., Fardin, M.-A., Mège, R.-M., Ladoux, B., Yap, A.S., Fanning, A.S., and Peifer, M. (2016). Remodeling the zonula adherens in response to tension and the role of afadin in this response. Journal of Cell Biology *213*, 243–260. https://doi.org/10.1083/jcb.201506115.

43. Gomez, G.A., McLachlan, R.W., and Yap, A.S. (2011). Productive tension: force-sensing and homeostasis of cell–cell junctions. Trends in Cell Biology *21*, 499–505. https://doi.org/10.1016/j.tcb.2011.05.006.

44. Yonemura, S. (2011). Cadherin-actin interactions at adherens junctions. Curr Opin Cell Biol *23*, 515–522. https://doi.org/10.1016/j.ceb.2011.07.001.

45. Sidor, C., Stevens, T.J., Jin, L., Boulanger, J., and Röper, K. (2020). Rho-Kinase Planar Polarization at Tissue Boundaries Depends on Phospho-regulation of Membrane Residence Time. Developmental Cell *52*, 364-378.e7. https://doi.org/10.1016/j.devcel.2019.12.003.

46. Wang, Y., and Riechmann, V. (2007). The Role of the Actomyosin Cytoskeleton in Coordination of Tissue Growth during Drosophila Oogenesis. Current Biology *17*, 1349–1355. https://doi.org/10.1016/j.cub.2007.06.067.

47. Sun, Y., Yan, Y., Denef, N., and Schüpbach, T. (2011). Regulation of somatic myosin activity by Protein Phosphatase 1β controls *Drosophila* oocyte polarization. Development *138*, 1991–2001. https://doi.org/10.1242/dev.062190.

48. Vereshchagina, N., Bennett, D., Gross, S., Vissi, E., White-Cooper, H., and Alphey, L. (2004). The Essential Role of PP1 beta in Drosophila Is to Regulate Nonmuscle Myosin. Molecular Biology of the Cell *15*.

49. Dawes-Hoang, R.E., Parmar, K.M., Christiansen, A.E., Phelps, C.B., Brand, A.H., and Wieschaus, E.F. (2007). *folded gastrulation* , cell shape change and the control of myosin localization. Development *134*, 4507–4507. https://doi.org/10.1242/dev.017343.

50. Ang, L.-H., Chen, W., Yao, Y., Ozawa, R., Tao, E., Yonekura, J., Uemura, T., Keshishian, H., and Hing, H. (2006). Lim kinase regulates the development of olfactory and neuromuscular synapses. Developmental Biology *293*, 178–190. https://doi.org/10.1016/j.ydbio.2006.01.030.

687 51. Fujiwara, I., Zweifel, M.E., Courtemanche, N., and Pollard, T.D. (2018). Latrunculin A
688 Accelerates Actin Filament Depolymerization in Addition to Sequestering Actin Monomers. Current
689 Biology *28*, 3183-3192.e2. https://doi.org/10.1016/j.cub.2018.07.082.

690 52. Cho, Y., Haraguchi, D., Shigetomi, K., Matsuzawa, K., Uchida, S., and Ikenouchi, J. (2022).
691 Tricellulin secures the epithelial barrier at tricellular junctions by interacting with actomyosin. Journal of
692 Cell Biology *221*, e202009037. https://doi.org/10.1083/jcb.202009037.

693 53. Gates, J., Mahaffey, J.P., Rogers, S.L., Emerson, M., Rogers, E.M., Sottile, S.L., Van Vactor,
694 D., Gertler, F.B., and Peifer, M. (2007). Enabled plays key roles in embryonic epithelial morphogenesis
695 in *Drosophila*. Development *134*, 2027–2039. https://doi.org/10.1242/dev.02849.

696 54. Manning, L.A., Perez-Vale, K.Z., Schaefer, K.N., Sewell, M.T., and Peifer, M. (2019). The
697 Drosophila Afadin and ZO-1 homologues Canoe and Polychaetoid act in parallel to maintain epithelial
698 integrity when challenged by adherens junction remodeling. MBoC *30*, 1938–1960.
699 https://doi.org/10.1091/mbc.E19-04-0209.

700 55. Ahern-Djamali, S.M., Comer, A.R., Bachmann, C., Kastenmeier, A.S., Reddy, S.K., Beckerle,
701 M.C., Walter, U., and Hoffmann, F.M. (1998). Mutations in Drosophila Enabled and Rescue by Human
702 Vasodilator-stimulated Phosphoprotein (VASP) Indicate Important Functional Roles for Ena/VASP
703 Homology Domain 1 (EVH1) and EVH2 Domains. MBoC *9*, 2157–2171.
704 https://doi.org/10.1091/mbc.9.8.2157.

705 56. Bear, J.E., Loureiro, J.J., Libova, I., Fässler, R., Wehland, J., and Gertler, F.B. (2000). Negative
706 Regulation of Fibroblast Motility by Ena/VASP Proteins. Cell *101*, 717–728.
707 https://doi.org/10.1016/S0092-8674(00)80884-3.

708 57. Higashi, T., Arnold, T.R., Stephenson, R.E., Dinshaw, K.M., and Miller, A.L. (2016).
709 Maintenance of the Epithelial Barrier and Remodeling of Cell-Cell Junctions during Cytokinesis. 1–15.

710 58. Izquierdo, E., Quinkler, T., and De Renzis, S. (2018). Guided morphogenesis through
711 optogenetic activation of Rho signalling during early Drosophila embryogenesis. Nature
712 Communications *9*, 2366. https://doi.org/10.1038/s41467-018-04754-z.

713 59. Oda, H., Uemura, T., Harada, Y., Iwai, Y., and Takeichi, M. (1994). A Drosophila Homolog of
714 Cadherin Associated with Armadillo and Essential for Embryonic Cell-Cell Adhesion. Developmental
715 Biology *165*, 716–726. https://doi.org/10.1006/DBIO.1994.1287.

716 60. Van Den Goor, L., Iseler, J., Koning, K.M., and Miller, A.L. (2024). Mechanosensitive recruitment
717 of Vinculin maintains junction integrity and barrier function at epithelial tricellular junctions. Current
718 Biology, S0960982224011758. https://doi.org/10.1016/j.cub.2024.08.060.

719 61. Alatortsev, V.E., Kramerova, I.A., Frolov, M.V., Lavrov, S.A., and Westphal, E.D. (1997).
720 *Vinculin* gene is non-essential in *Drosophila melanogaster*. FEBS Letters *413*, 197–201.
721 https://doi.org/10.1016/S0014-5793(97)00901-0.

722 62. Maartens, A.P., Wellmann, J., Wictome, E., Klapholz, B., Green, H., and Brown, N.H. (2016).
723 Drosophila vinculin is more harmful when hyperactive than absent, and can circumvent integrin to form
724 adhesion complexes. J Cell Sci *129*, 4354–4365. https://doi.org/10.1242/jcs.189878.

725 63. Rauskolb, C., Cervantes, E., Madere, F., and Irvine, K.D. (2019). Organization and function of
726 tension-dependent complexes at adherens junctions. Journal of Cell Science *132*, jcs224063.
727 https://doi.org/10.1242/jcs.224063.

728 64. Leerberg, J.M., Gomez, G.A., Verma, S., Moussa, E.J., Wu, S.K., Priya, R., Hoffman, B.D.,
729 Grashoff, C., Schwartz, M.A., and Yap, A.S. (2014). Tension-Sensitive Actin Assembly Supports
730 Contractility at the Epithelial Zonula Adherens. Current Biology *24*, 1689–1699.
731 https://doi.org/10.1016/j.cub.2014.06.028.

732 65. Nowotarski, S.H., McKeon, N., Moser, R.J., and Peifer, M. (2014). The actin regulators Enabled
733 and Diaphanous direct distinct protrusive behaviors in different tissues during *Drosophila* development.
734 MBoC *25*, 3147–3165. https://doi.org/10.1091/mbc.e14-05-0951.

735 66. Arber, S., Barbayannis, F.A., Hanser, H., Schneider, C., Stanyon, C.A., Bernard, O., and Caroni,
736 P. (1998). Regulation of actin dynamics through phosphorylation of cofilin by LIM-kinase. Nature *393*,
737 805–809. https://doi.org/10.1038/31729.

738 67. Rana, M.K., and Worthylake, R.A. (2012). Novel Mechanism for Negatively Regulating Rho-
739 Kinase (ROCK) Signaling through Coronin1B Protein in Neuregulin 1 (NRG-1)-induced Tumor Cell

Motility. Journal of Biological Chemistry *287*, 21836–21845. https://doi.org/10.1074/jbc.M112.346114.

68. Claesson-Welsh, L., Dejana, E., and McDonald, D.M. (2021). Permeability of the Endothelial Barrier: Identifying and Reconciling Controversies. Trends in Molecular Medicine *27*, 314–331. https://doi.org/10.1016/j.molmed.2020.11.006.

69. Kugelmann, D., Rotkopf, L.T., Radeva, M.Y., Garcia-Ponce, A., Walter, E., and Waschke, J. (2018). Histamine causes endothelial barrier disruption via Ca2+-mediated RhoA activation and tension at adherens junctions. Sci Rep *8*, 13229. https://doi.org/10.1038/s41598-018-31408-3.

70. Waschke, J., Baumgartner, W., Adamson, R.H., Zeng, M., Aktories, K., Barth, H., Wilde, C., Curry, F.E., and Drenckhahn, D. (2004). Requirement of Rac activity for maintenance of capillary endothelial barrier properties. American Journal of Physiology-Heart and Circulatory Physiology *286*, H394–H401. https://doi.org/10.1152/ajpheart.00221.2003.

71. Meltzer, H., Marom, E., Alyagor, I., Mayseless, O., Berkun, V., Segal-Gilboa, N., Unger, T., Luginbuhl, D., and Schuldiner, O. (2019). Tissue-specific (ts)CRISPR as an efficient strategy for in vivo screening in Drosophila. Nat Commun *10*, 2113. https://doi.org/10.1038/s41467-019-10140-0.

72. Riedl, J., Crevenna, A.H., Kessenbrock, K., Yu, J.H., Neukirchen, D., Bista, M., Bradke, F., Jenne, D., Holak, T.A., Werb, Z., et al. (2008). Lifeact: a versatile marker to visualize F-actin. Nat Methods *5*, 605–607. https://doi.org/10.1038/nmeth.1220.

73. Zhang, H., Lesnov, G.D., Subach, O.M., Zhang, W., Kuzmicheva, T.P., Vlaskina, A.V., Samygina, V.R., Chen, L., Ye, X., Nikolaeva, A.Yu., et al. (2024). Bright and stable monomeric green fluorescent protein derived from StayGold. Nat Methods *21*, 657–665. https://doi.org/10.1038/s41592-024-02203-y.

74. Bischof, J., Maeda, R.K., Hediger, M., Karch, F., and Basler, K. (2007). An optimized transgenesis system for Drosophila using germ-line-specific phiC31 integrases. Proc Natl Acad Sci U S A *104*, 3312–3317. https://doi.org/10.1073/pnas.0611511104.

75. Doerflinger, H., Zimyanin, V., and St Johnston, D. (2022). The Drosophila anterior-posterior axis is polarized by asymmetric myosin activation. Current Biology *32*, 374-385.e4. https://doi.org/10.1016/j.cub.2021.11.024.

76. Sutcliffe, B., Ng, J., Auer, T.O., Pasche, M., Benton, R., Jefferis, G.S.X.E., and Cachero, S. (2017). Second-Generation *Drosophila* Chemical Tags: Sensitivity, Versatility, and Speed. Genetics *205*, 1399–1408. https://doi.org/10.1534/genetics.116.199281.

77. Hannaford, M., Loyer, N., Tonelli, F., Zoltner, M., and Januschke, J. (2019). A chemical-genetics approach to study the role of atypical protein kinase C in *Drosophila*. Development, dev.170589. https://doi.org/10.1242/dev.170589.

78. Schindelin, J., Arganda-Carreras, I., Frise, E., Kaynig, V., Longair, M., Pietzsch, T., Preibisch, S., Rueden, C., Saalfeld, S., Schmid, B., et al. (2012). Fiji: an open-source platform for biological-image analysis. Nature Methods *9*, 676–682. https://doi.org/10.1038/nmeth.2019.

79. Allan, C., Burel, J.-M., Moore, J., Blackburn, C., Linkert, M., Loynton, S., MacDonald, D., Moore, W.J., Neves, C., Patterson, A., et al. (2012). OMERO: flexible, model-driven data management for experimental biology. Nat Methods *9*, 245–253. https://doi.org/10.1038/nmeth.1896.

80. Holm, S. (1979). A Simple Sequentially Rejective Multiple Test Procedure. Scandinavian Journal of Statistics *6*, 65–70.

Figure 1

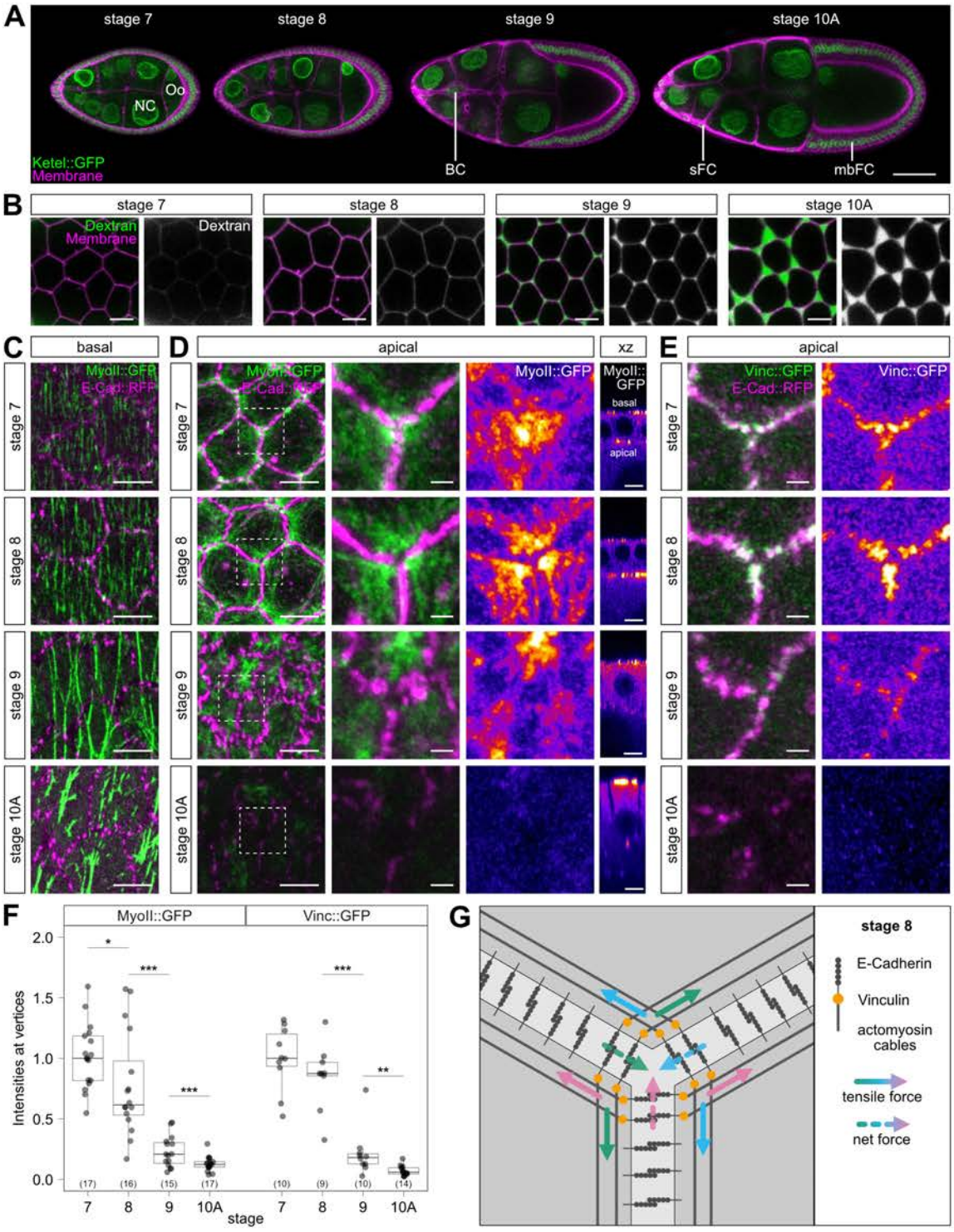
A
stage 7
stage 8
stage 9
stage 10A
Oo
NC
Ketel::GFP
Membrane
BC
sFC
mbFC
B
stage 7
stage 8
stage 9
stage 10A
Dextran
Membrane
Dextran
C
basal
D
apical
xz
E
apical
MyoII::GFP
E-Cad::RFP
Vinc::GFP
basal
apical
stage 7
stage 8
stage 9
stage 10A
F
MyoII::GFP
Vinc::GFP
Intensities at vertices
stage
G
stage 8
E-Cadherin
Vinculin
actomyosin cables
tensile force
net force

783 **Figure 1**

784 **Reorganization of actomyosin at follicle cell vertices precedes vertex opening.**

785 **(A)** Confocal sections of living follicles before (stage 7) and during (stages 8, 9, 10A)
786 vitellogenesis. Fs(2)Ket::GFP (green) labels nuclei, CellMask (magenta) labels plasma
787 membranes. Anterior is to the left, dorsal is up. NC, nurse cells; Oo, oocyte; BC, border cells;
788 sFC, stretch follicle cells; mbFC, main body follicle cells.

789 **(B)** Basolateral sections of mbFCs acquired at 25% FC height. Dextran (green) marks
790 intercellular spaces, CellMask (magenta) labels plasma membranes. Single-channel views
791 show dextran (grey).

792 **(C-D)** Basal (C) and apical (D) sections of mbFCs expressing E-Cad::RFP (magenta) and
793 MyoII::GFP (green). Close-ups (D) show single vertices (rectangles in overview). Note that
794 MyoII (intensities color-coded using heatmap in (D)) accumulates near apical vertices at stage
795 7 and 8 and redistributes to the medial region at stage 9 (D). Cross-sectional (xz) view (D)
796 shows that apical, but not basal, MyoII declines by stage 9.

797 **(E)** Apical sections of FC vertices in follicles expressing E-Cad::RFP (magenta) and Vinc::GFP
798 (green). Note that Vinc::GFP (color-coded using heatmap in single-channel view) accumulates
799 near vertices at stage 7 and 8 and declines by stage 9.

800 **(F)** Quantification of MyoII::GFP and Vinc::GFP signals (normalized) at apical vertices. Box
801 plots show maximum and minimum observations, upper and lower quartile, and median
802 (horizontal line). Number of follicles (n) analyzed is indicated. P-values (Pairwise Wilcoxon
803 Rank Sum Test): * $p \leq 0.05$, ** $p \leq 0.01$, *** $p \leq 0.001$, **** $p \leq 0.0001$.

804 **(G)** Model of force transmission at apical FC vertices at stage 8 (modified from [19]).

805 Scale bars: (A), 50 µm; (B- D), 5 µm, close-ups 1 µm, (E) 1 µm.

806 See also Figure S1 and Video S1.

807

Figure 2

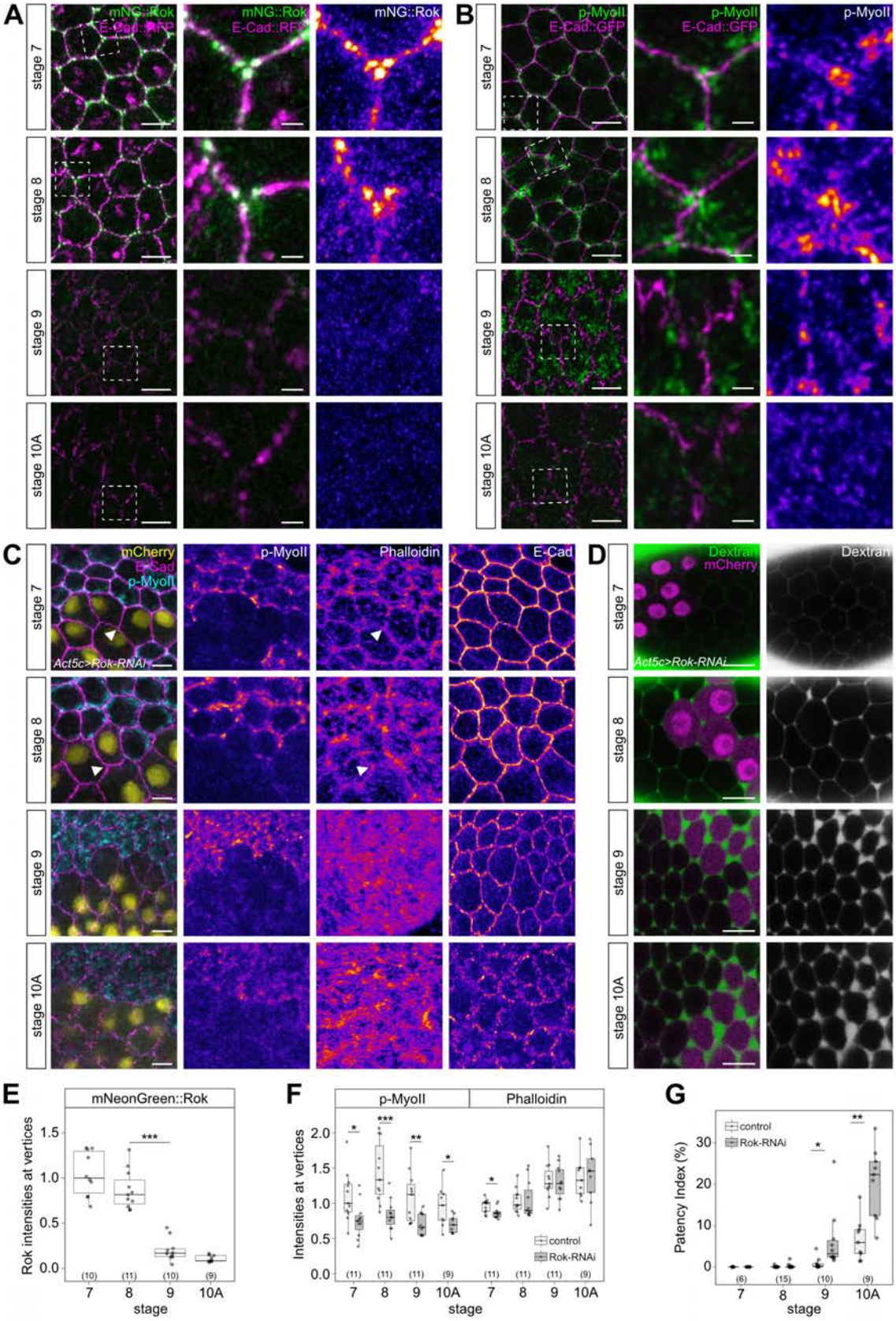
A
mNG::Rok
E-Cad::RFP
mNG::Rok
E-Cad::RFP
mNG::Rok
B
p-MyoII
E-Cad::GFP
p-MyoII
E-Cad::GFP
p-MyoII
stage 7
stage 8
stage 9
stage 10A
C
mCherry
E-Cad
p-MyoII
p-MyoII
Phalloidin
E-Cad
Act5c>Rok-RNAi
D
Dextran
mCherry
Dextran
Act5c>Rok-RNAi
E
mNeonGreen::Rok
Rok intensities at vertices
stage
F
p-MyoII
Phalloidin
Intensities at vertices
control
Rok-RNAi
stage
G
control
Rok-RNAi
Patency Index (%)
stage

809 **Figure 2**

810 **Rho-associated kinase localizes at follicle cell vertices and limits vertex opening.**

811 **(A)** Apical sections of mbFCs expressing E-Cad::RFP (magenta) and mNeonGreen::Rok
812 (mNG::Rok; green). Close-up views show single vertices. Note that mNG::Rok (intensities
813 color-coded using heatmap in single-channel view) accumulates near vertices in pre-patent
814 follicles (stage 7, 8), but not in later stages.

815 **(B)** Apical sections of follicles expressing E-Cad::GFP (magenta) stained for p-MyoII (green;
816 heatmap in single-channel view). Close-ups show single vertices. Note that p-MyoII
817 redistributes from vertices to the medial region by stage 9.

818 **(C)** Apical sections of follicles expressing *Rok* dsRNA in mCherry-nls-marked clones (yellow)
819 stained for p-MyoII (cyan), E-Cad (magenta) and F-actin (Phalloidin; not shown in merge).
820 Note reduced p-MyoII, but not F-actin signals in Rok-depleted cells. Arrowheads indicate F-
821 actin accumulation at vertices in Rok-depleted cells.

822 **(D)** Basolateral sections of follicles expressing *Rok* dsRNA in mCherry-nls-marked clones
823 (magenta). Dextran (green) marks intercellular spaces. Single-channel views show dextran
824 (grey). Note enlarged gaps in Rok-depleted cells compared to control cells at stage 9 and
825 stage 10A.

826 **(E)** Quantification of mNeonGreen::Rok signals (normalized) at apical vertices. Number of
827 follicles (n) analyzed is indicated. P-values (Pairwise Wilcoxon Rank Sum Test): * $p \leq 0.05$, **
828 $p \leq 0.01$, *** $p \leq 0.001$, **** $p \leq 0.0001$.

829 **(F)** Quantification of p-MyoII and Phalloidin signals (normalized) at apical vertices in *Rok* RNAi
830 and control clones. Number of follicles (n) analyzed is indicated. P-values (Welch's two-sample
831 t-test): * $p \leq 0.05$, ** $p \leq 0.01$, *** $p \leq 0.001$, **** $p \leq 0.0001$.

832 **(G)** Quantification of patency index in *Rok* RNAi and control clones. Number of follicles (n)
833 analyzed is indicated. P-values (Welch's two-sample t-test): * $p \leq 0.05$, ** $p \leq 0.01$, *** $p \leq$
834 0.001, **** $p \leq 0.0001$.

835 Scale bars: (A-B), 5 µm, close-ups 1 µm; (C) 5 µm; (D) 10 µm.

836 See also Figures S2 and S3.

837

838

839

840

Figure 3

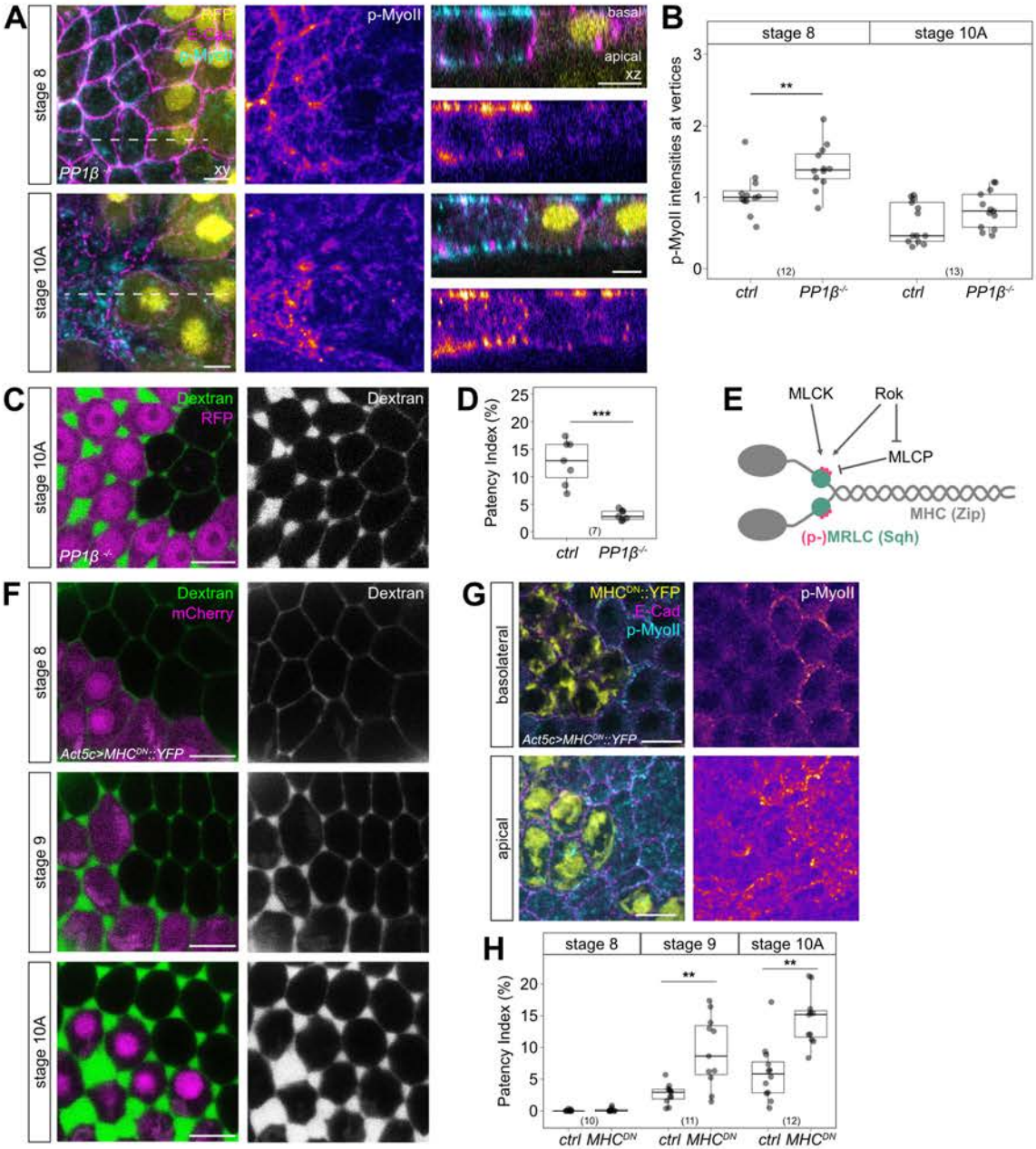
A
stage 8
stage 10A
RFP
E-Cad
p-MyoII
PP1β -/-
xy
p-MyoII
basal
apical
xz
B
stage 8
stage 10A
p-MyoII intensities at vertices
**
(12)
(13)
ctrl
PP1β-/-
ctrl
PP1β-/-
C
stage 10A
Dextran
RFP
PP1β -/-
Dextran
D
Patency Index (%)
***
(7)
ctrl
PP1β-/-
E
MLCK
Rok
MLCP
MHC (Zip)
(p-)MRLC (Sqh)
F
stage 8
stage 9
stage 10A
Dextran
mCherry
Act5c>MHCDN::YFP
Dextran
G
basolateral
apical
MHCDN::YFP
E-Cad
p-MyoII
Act5c>MHCDN::YFP
p-MyoII
H
stage 8
stage 9
stage 10A
Patency Index (%)
**
**
(10)
(11)
(12)
ctrl MHCDN
ctrl MHCDN
ctrl MHCDN

842 **Figure 3**

843 **Downregulation of Myosin II activity by protein phosphatase 1 is required for patency.**

844 **(A)** Apical (xy, left) and orthogonal (xz, right) sections of follicle epithelium carrying *PP1β*
845 (*flw*^{FP41}) clones (marked by absence of RFP (yellow)), stained for E-Cad (magenta) and p-
846 MyoII (cyan). Dashed lines indicate positions of orthogonal sections. Note increased p-MyoII
847 levels (color-coded using heatmap) on apical and basal sides in *PP1β* mutant cells.

848 **(B)** Quantification of p-MyoII signals (normalized) at apical vertices in *PP1β* and control cells.
849 Number of follicles (n) analyzed is indicated. P-values (Welch's two-sample t-test): * $p \leq 0.05$,
850 ** $p \leq 0.01$, *** $p \leq 0.001$, **** $p \leq 0.0001$.

851 **(C)** Basolateral section of follicle carrying *PP1β* clone marked by absence of RFP (magenta).
852 Dextran (green) marks intercellular spaces.

853 **(D)** Quantification of patency index of *PP1β* and control cells. Number of follicles (n) analyzed
854 is indicated. P-values (Welch's two-sample t-test): * $p \leq 0.05$, ** $p \leq 0.01$, *** $p \leq 0.001$, **** p
855 ≤ 0.0001.

856 **(E)** Scheme of non-muscle Myosin II with Myosin heavy chain (MHC/Zip), Myosin regulatory
857 light chain (MRLC/Sqh), and its regulators Myosin light chain kinase (MLCK), Myosin light-
858 chain phosphatase (MLCP), and Rok.

859 **(F)** Basolateral sections of mbFCs expressing MHC^{DN}::YFP in mCherry-nls-marked clones
860 (magenta). Dextran (green) marks intercellular spaces. Note enlarged intercellular gaps in
861 MHC^{DN}::YFP-expressing tissue at stage 9 and 10A.

862 **(G)** Stage 10A follicle expressing MHC^{DN}::YFP (yellow) in clones, stained for E-Cad (magenta)
863 and p-MyoII (cyan). Note that MHC^{DN}::YFP-expressing cells show reduced p-MyoII levels.

864 **(H)** Patency index of control and MHC^{DN}::YFP-expressing clones. Number of follicles (n)
865 analyzed is indicated. P-values (Welch's two-sample t-test): * $p \leq 0.05$, ** $p \leq 0.01$, *** $p \leq$
866 0.001, **** $p \leq 0.0001$.

867 Scale bars: (A) 5 µm; (C,F,G) 10 µm.

868 See also Figure S3.

869

870

871

872

873

Figure 4

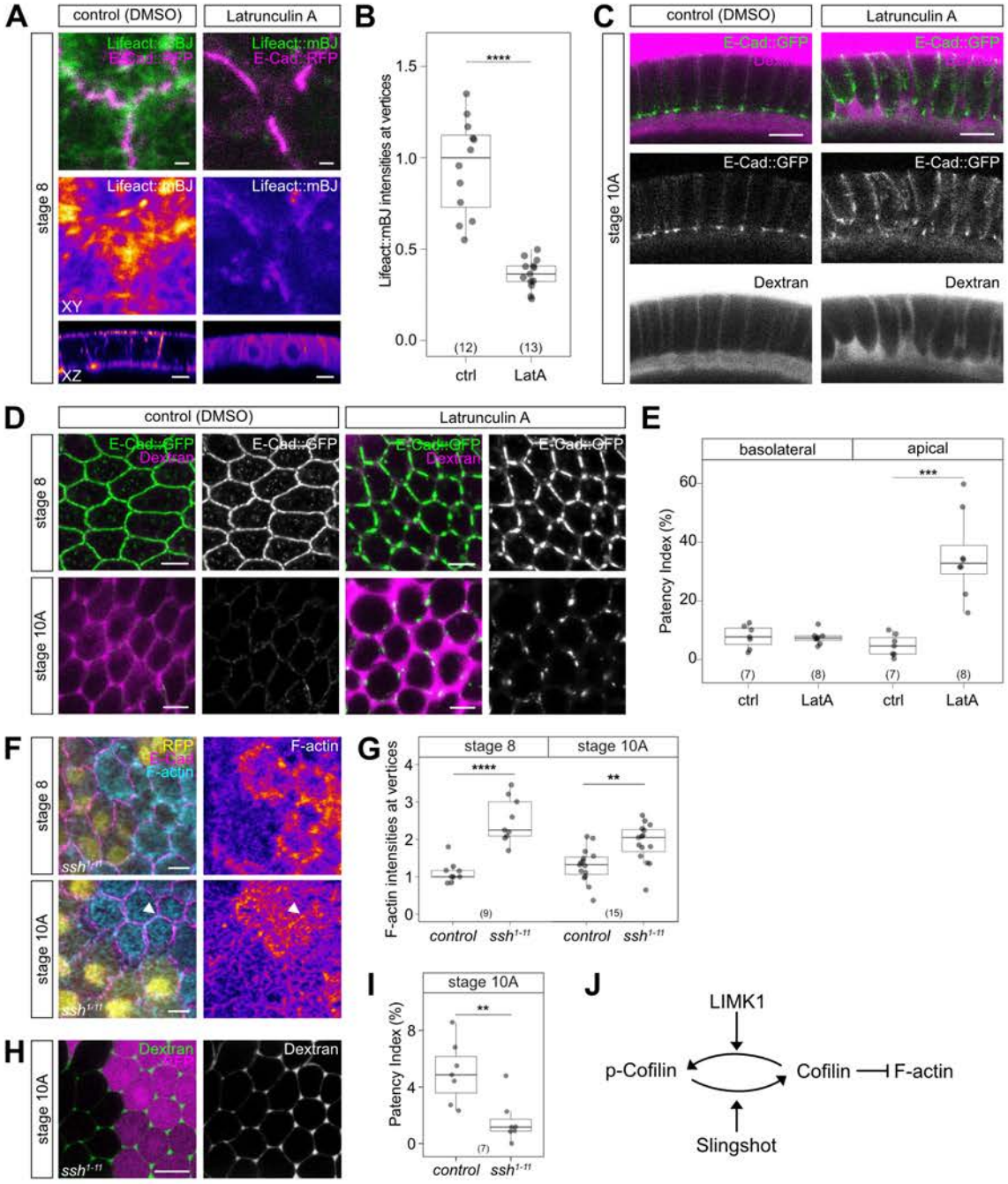
A
control (DMSO)
Latrunculin A
stage 8
Lifeact::mBJ
E-Cad::RFP
XY
XZ
B
Lifeact::mBJ intensities at vertices
****
(12)
(13)
ctrl
LatA
C
control (DMSO)
Latrunculin A
stage 10A
E-Cad::GFP
Dextran
D
control (DMSO)
Latrunculin A
stage 8
stage 10A
E-Cad::GFP
Dextran
E
basolateral
apical
Patency Index (%)
***
(7)
(8)
(7)
(8)
ctrl
LatA
ctrl
LatA
F
stage 8
stage 10A
RFP
E-Cad
F-actin
ssh1-11
G
stage 8
stage 10A
F-actin intensities at vertices
****
**
(9)
(15)
control
ssh1-11
control
ssh1-11
H
stage 10A
Dextran
ssh1-11
I
stage 10A
Patency Index (%)
**
(7)
control
ssh1-11
J
LIMK1
p-Cofilin
Cofilin
F-actin
Slingshot

875 **Figure 4**

876 **F-actin dynamics regulates vertex opening.**

877 **(A)** Apical (xy, top) or orthogonal (xz, bottom) sections of stage 8 follicles expressing E-
878 Cad::RFP (magenta) and Lifeact::mBaoJin (green), treated with DMSO (1%, control) or
879 Latrunculin A (LatA; 2 µM). Note reduced Lifeact::mBaoJin intensities after LatA treatment.

880 **(B)** Quantification of Lifeact::mBaoJin signals (normalized) at apical vertices of stage 8 follicles
881 treated with DMSO (control) or LatA. Number of follicles (n) analyzed is indicated. P-values
882 (Welch's two-sample t-test): * $p \leq 0.05$, ** $p \leq 0.01$, *** $p \leq 0.001$, **** $p \leq 0.0001$.

883 **(C)** Cross-sections of stage 10A follicles expressing E-Cad::GFP (green) treated with DMSO
884 (control) or LatA. Single channels show E-Cad or Dextran (grey). Note enlarged intercellular
885 gaps filled with dextran (magenta) on apical side in LatA-treated follicles.

886 **(D)** Apical sections of mbFCs expressing E-Cad::GFP. Follicles were treated with DMSO
887 (control) or 2 µM LatA for 45 minutes before imaging. Single channels show E-Cad (grey).
888 Note removal of E-Cad from vertices and enlarged intercellular gaps filled with dextran
889 (magenta) in LatA-treated follicles.

890 **(E)** Patency index on basolateral and apical sides of stage 10A follicles treated with DMSO
891 (control) or LatA. Number of follicles (n) analyzed is indicated. P-values (Welch's two-sample
892 t-test): * $p \leq 0.05$, ** $p \leq 0.01$, *** $p \leq 0.001$, **** $p \leq 0.0001$.

893 **(F)** Apical sections of mbFCs carrying *ssh*$^{1-11}$ clones (marked by absence of RFP (yellow)),
894 stained for E-Cad (magenta) and p-MyoII (cyan). Note accumulation of p-MyoII at vertices at
895 stage 10A (arrowheads).

896 **(G)** Quantification of Phalloidin signals (normalized) at apical vertices in *ssh*$^{1-11}$ and control
897 cells at stage 8 and stage 10A. Number of follicles (n) analyzed is indicated. P-values (Welch's
898 two-sample t-test): * $p \leq 0.05$, ** $p \leq 0.01$, *** $p \leq 0.001$, **** $p \leq 0.0001$.

899 **(H)** Basolateral section of follicle carrying *ssh*$^{1-11}$ clone marked by absence of RFP (magenta).
900 Dextran (green) marks intercellular spaces.

901 **(I)** Patency index in *ssh*$^{1-11}$ clones and control cells. Number of follicles (n) analyzed is
902 indicated. P-values (Welch's two-sample t-test): * $p \leq 0.05$, ** $p \leq 0.01$, *** $p \leq 0.001$, **** $p \leq$
903 0.0001.

904 **(J)** Scheme of Cofilin regulation. Phosphorylation by LIMK1 inactivates, while
905 dephosphorylation by Slingshot activates Cofilin´s F-actin depolymerizing activity.

906 Scale bars: (A) 1 µm; (C,H) 10 µm; (D,F) 5 µm.

907 See also Figures S3 and S4.

Figure 5

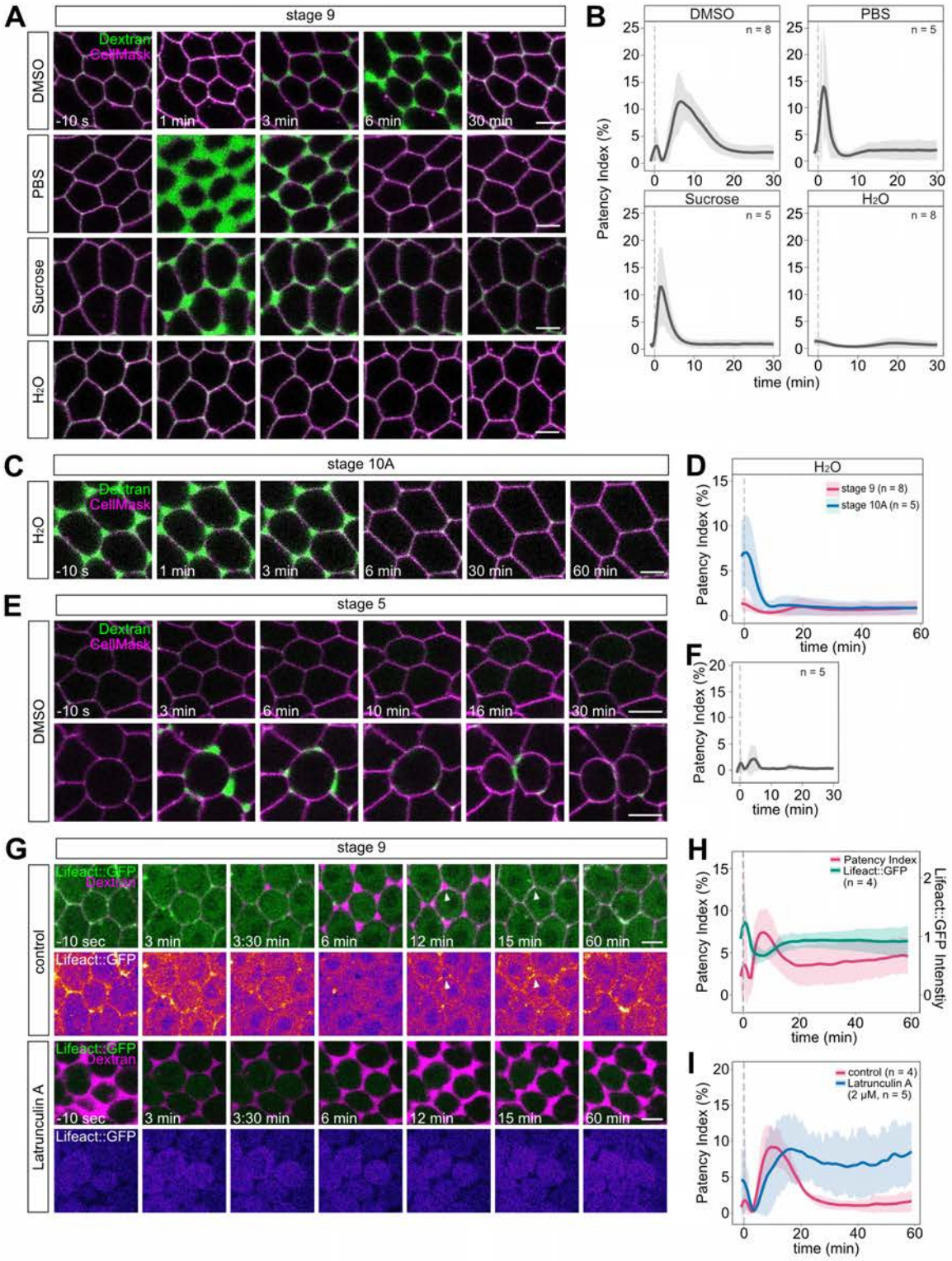
A
stage 9
DMSO
PBS
Sucrose
H2O
Dextran
CellMask
-10 s
1 min
3 min
6 min
30 min
B
DMSO
PBS
Sucrose
H2O
n = 8
n = 5
Patency Index (%)
time (min)
C
stage 10A
60 min
D
stage 9 (n = 8)
stage 10A (n = 5)
E
stage 5
10 min
16 min
F
G
stage 9
control
Latrunculin A
Lifeact::GFP
Dextran
-10 sec
3:30 min
12 min
15 min
H
Patency Index
Lifeact::GFP (n = 4)
Lifeact::GFP Intensity
I
control (n = 4)
Latrunculin A (2 µM, n = 5)

Figure 5

Hypertonic shock induces opening of follicle cell vertices *ex vivo.*

(A) Stills (basolateral sections) from time-lapse movies of early patent (stage 9) follicles exposed to hypertonic (305 mosmol/L / 2.38% DMSO, 88,96 mosmol/L / 0.238x PBS, or 50 mosmol/L / 50 mM Sucrose) or hypotonic (50% H_2O) medium at t=0 min. Dextran (green) marks intercellular spaces, CellMask (magenta) labels plasma membranes.

(B) Patency index over time after hypertonic or hypotonic treatment as indicated. Graphs show mean values and standard deviations, smoothed using a running median.

(C) Basolateral sections of patent (stage 10A) follicle exposed to hypotonic (50% H_2O) medium at t=0 min. Note that intercellular gaps close after addition of H_2O.

(D) Patency index over time after hypotonic treatment of stage 9 (purple line) or stage 10A (blue line) follicles.

(E) Hypertonic (DMSO) treatment of stage 5 follicles. Note that vertices of interphase cells remain closed after adding DMSO (top), whereas transient leaks appear at boundaries of dividing cells (bottom).

(F) Patency index over time of stage 5 follicles.

(G) Stage 9 follicles expressing Lifeact::GFP (driven by *CY2*-Gal4; green), treated with DMSO (control; top) or 2 µM LatA (bottom) for 45 minutes before imaging. Dextran (magenta) marks intercellular spaces. At t=0 min, follicles were exposed to DMSO-induced hypertonic shock. Note that Lifeact::GFP disappears before gap opening and relocalizes at vertices (arrowheads) when gaps start to close. Open vertices fail to close in LatA-treated follicles.

(H) Quantification of Lifeact::GFP signals at cell boundaries (green line) and of patency index (purple line) over time in control follicles.

(I) Patency index over time of control (purple line) and LatA-treated (blue line) follicles.

Scale bars: (A, C, E, G): 5 µm.

See also Videos S2, S3, S4 and S5.

Figure 6

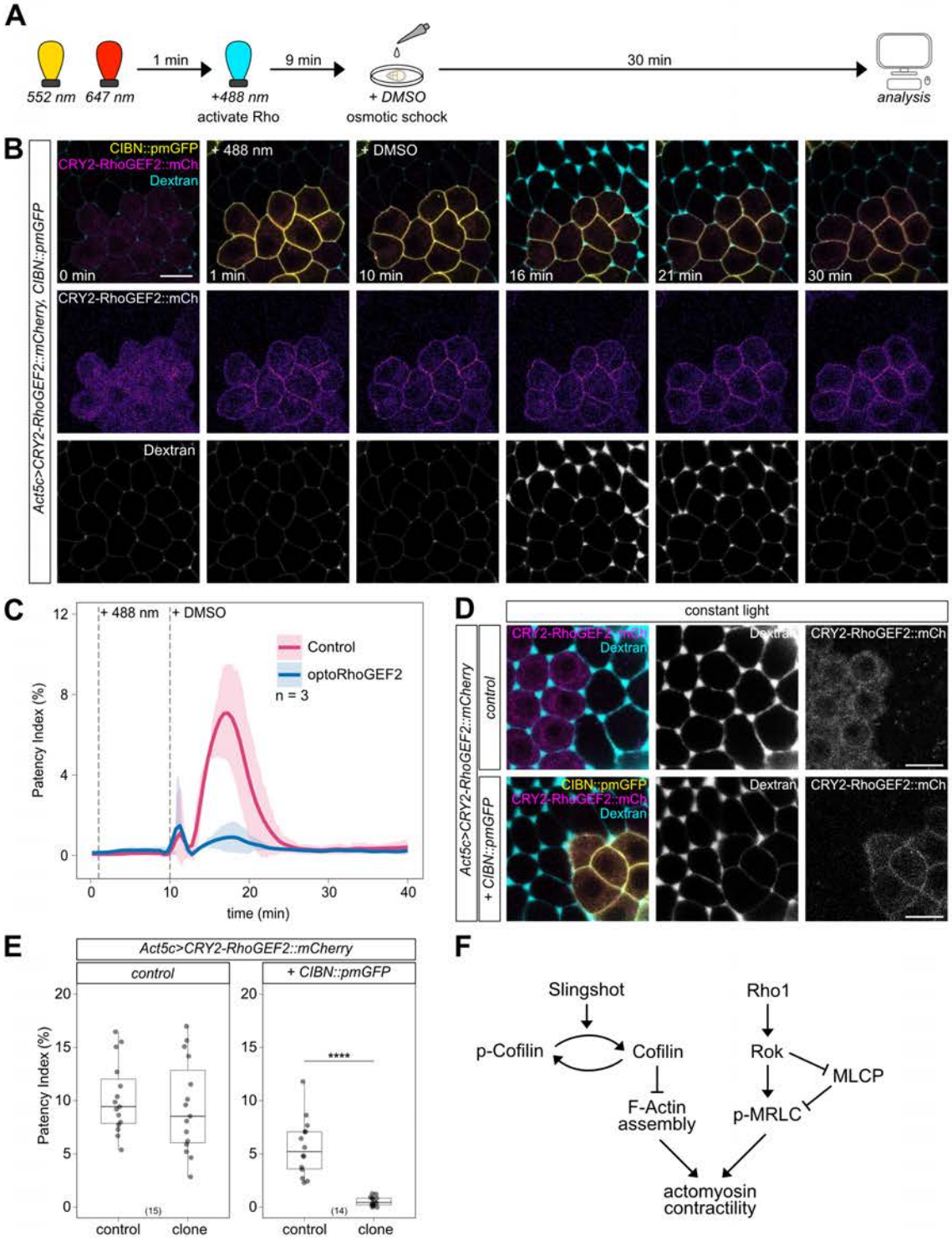
A
552 nm
647 nm
1 min
+488 nm
activate Rho
9 min
+ DMSO
osmotic schock
30 min
analysis
B
Act5c>CRY2-RhoGEF2::mCherry, CIBN::pmGFP
CIBN::pmGFP
CRY2-RhoGEF2::mCh
Dextran
+ 488 nm
+ DMSO
0 min
1 min
10 min
16 min
21 min
30 min
CRY2-RhoGEF2::mCh
Dextran
C
+ 488 nm
+ DMSO
Control
optoRhoGEF2
n = 3
Patency Index (%)
time (min)
D
constant light
Act5c>CRY2-RhoGEF2::mCherry
control
+ CIBN::pmGFP
CRY2-RhoGEF2::mCh
Dextran
CIBN::pmGFP
E
Act5c>CRY2-RhoGEF2::mCherry
control
+ CIBN::pmGFP
Patency Index (%)
****
control
clone
F
Slingshot
Rho1
p-Cofilin
Cofilin
Rok
MLCP
F-Actin assembly
p-MRLC
actomyosin contractility

941

942 **Figure 6**

943 **Acute activation of Rho is sufficient to prevent patency.**

944 **(A)** Scheme of combined Rho activation and hypertonic shock experiment. Follicles are
945 exposed to blue light (488 nm, 9 min) to activate Rho signaling before adding DMSO at t=10
946 min to induce a hypertonic shock.

947 **(B)** Stills (basolateral sections) from time-lapse movie of stage 9 follicle expressing CRY2-
948 RhoGEF2::mCherry (magenta) and CIBN::pmGFP (yellow) in FC clone. Dextran (cyan) marks
949 intercellular spaces. Blue light at t=1 min (+488 nm) triggers membrane localization of CRY2-
950 RhoGEF2::mCherry. DMSO-induced hypertonic shock at t=10 min triggers vertex opening in
951 control tissue, whereas vertices of optoRhoGEF-expressing cells do not open. Single channels
952 show CRY2-RhoGEF2::mCherry intensities (heat map) and dextran (grey).

953 **(C)** Patency index over time of control cells (purple line) and optoRhoGEF-expressing cells
954 (blue line). Mean values and standard deviations (smoothed using a running median) are
955 shown.

956 **(D)** Basolateral sections of stage 10A follicles from females raised in constant light, expressing
957 CRY2-RhoGEF2::mCherry (magenta) either alone (top) or with CIBN::pmGFP (yellow, bottom)
958 in FC clones. Note that continuous Rho activation by plasma-membrane-targeted RhoGEF2,
959 but not overexpressed RhoGEF2 alone, blocks vertex opening.

960 **(E)** Patency index of FCs expressing CRY2-RhoGEF2::mCherry either alone (left) or together
961 with CIBN::pmGFP (right) under constant light. Act5c>CRY2-RhoGEF2::mCherry-expressing
962 cells ("clone") are compared to surrounding cells ("control"). Number of follicles (n) analyzed
963 is indicated. P-values (Welch's two-sample t-test): * $p \leq 0.05$, ** $p \leq 0.01$, *** $p \leq 0.001$, **** p
964 ≤ 0.0001.

965 **(F)** Regulation of actomyosin contractility in FCs at patency initiation.

966 Scale bars: (B, D) 10 µm.

967 See also Video S6.